The Milky Way's Dwarf Satellite Galaxies in ΛCDM: Orbital Ellipticities and Internal Structure

by

Christopher Barber
BSc, Queen's University, 2011

A Thesis Submitted in Partial Fulfillment of the
Requirements for the Degree of

MASTER OF SCIENCE

in the Department of Physics and Astronomy

The Milky Way's Dwarf Satellite Galaxies in ΛCDM:
Orbital Ellipticities and Internal Structure

by

Christopher Barber
BSc, Queen's University, 2011

Supervisory Committee

Prof. J. F. Navarro, Supervisor
(Department of Physics and Astronomy)

Assoc. Prof. K. Venn, Departmental Member
(Department of Physics and Astronomy)

Supervisory Committee

Prof. J. F. Navarro, Supervisor
(Department of Physics and Astronomy)

Assoc. Prof. K. Venn, Departmental Member
(Department of Physics and Astronomy)

ABSTRACT

Current models of cosmology and galaxy formation are possibly at odds with observations of small-scale galaxies. Such is the case for the dwarf spheroidal (dSph) galaxies of the Milky Way (MW), where tension exists in explaining their observed abundance, mass, and internal structure. Here we present an analysis of the substructure surrounding MW-sized haloes in a Λ Cold Dark Matter (ΛCDM) simulation suite. Combined with a semi-analytic model of galaxy formation and evolution, we identify substructures that are expected to host dSph galaxies similar to the satellites of the MW. We subsequently use these simulations to investigate the orbital properties of dSph satellite galaxies to make contact with those orbiting the MW. After accretion into the main halo, the higher mass "luminous" substructure remains on highly radial orbits while the orbits of lower mass substructure, which are not expected to host stars, tend to scatter off of the luminous substructure, and thus circularize over time. The orbital ellipticity distribution of the luminous substructure shows little dependence on the mass or formation history of the main halo, making this distribution a robust prediction of ΛCDM. Through comparison with the ellipticity distribution computed from the positions and velocities of the nine MW dSph galaxies that currently have proper motion estimates as a function of the assumed MW mass, we present a novel means of estimating the virial mass of the Milky Way. The best match is obtained assuming a mass of $1.1 \times 10^{12}\,\mathrm{M}_{\odot}$ with 95 per cent confidence limits of $(0.6 - 3.1) \times 10^{12}\,\mathrm{M}_{\odot}$. The uncertainty in this estimate is dominated by the large uncertainties in the proper motions and small number of MW satellites used, and will improve significantly with better proper motion measurements from Gaia.

We also measure the shape of the gravitational potential of subhaloes likely to host dSphs, down to radii comparable to the half-light radii of MW dSphs. Field haloes are triaxial in general, while satellite haloes become more spherical over time due to tidal interactions with the host. Thus through the determination of the shape of a MW dSph's gravitational potential via line of sight velocity measurements, one could in principle deduce the impact of past tidal interactions with the MW, and thus determine its dynamical history. Additionally, luminous subhaloes experience a radial alignment of their major axes with the direction to the host halo over time, caused by tidal torquing with the host's gravitational potential during close pericentric passages. This effect is seen at all radii, even down to the half-light radii of the satellites. Radial alignment must be taken into account when calibrating weak-lensing surveys which often assume isotropic orientations of satellite galaxies surrounding host galaxies and clusters.

Contents

List of Tables

List of Figures

ACKNOWLEDGEMENTS

I would like to thank:

My supervisor, Julio Navarro, for his constant support, encouragement, availability, patience, and "cotton candy" attitude that made our meetings both fun and productive. His vast knowledge and expertise was essential in keeping me constantly on track, especially when overcoming difficult obstacles in my research.

My committee, for their extremely helpful questions and suggestions regarding my thesis.

Else, for all of her extremely helpful suggestions and insight during our meetings, as well as help in the writing of the thesis. Her incredible, limitless amount of patience and encouragement combined with an extremely positive attitude toward astronomy really helped motivate me when the answer felt about as close as UDFj-39546284. I couldn't have done it without you!

Charli, Jason, and Azi, for the extremely helpful mock defence, and being awesome friends in general.

My officemates throughout the years: Azi, Christian, Cory, Hannah, Kyle, Razzi, "Cool" Chris Bildfell, Sheona, and J.C., for the nearly constant, much needed distractions and laughs when we've all been working just a little too hard.

Harjit the janitor, for reminding me to go home when I'm the last one in the office at the end of a long, frustrating day.

Azi, for being the best officemate of all time, and eating my leftover bananas at the end of every week.

Zoë, for being a peach.

DEDICATION

To my feet, may they take me where I need to go.

Chapter 1

Introduction

Recognize that the very molecules that make up your body, the atoms that construct the molecules, are traceable to the crucibles that were once the centers of high mass stars that exploded their chemically rich guts into the galaxy, enriching pristine gas clouds with the chemistry of life. So that we are all connected to each other biologically, to the earth chemically and to the rest of the Universe atomically. That's kinda cool! That makes me smile and I actually feel quite large at the end of that. It's not that we are better than the Universe, we are part of the Universe. We are in the Universe and the Universe is in us.

– Neil deGrasse Tyson

1.1 Dwarf Galaxies

The night sky is filled with wonders. Even from the city of Victoria, constellations of stars, planets, and star clusters will appear to the casual observer on those rare cloudless nights. However, as is almost always the case in astronomy, there is often much more than meets the eye. As one moves away from the city lights, other objects begin to appear: fainter stars, the beautiful arcing band of our Milky Way (MW) galaxy, along with other strange, fuzzier objects. Baffled by the fuzzy objects for centuries, astronomers referred to them simply as "nebulae", and believed them to reside within the MW. It wasn't until the 1920's that they began to consider the notion that some of these nebulae are in fact "island universes"; galaxies, some just like our own MW, that lie far beyond the reaches of our own Galactic disc.

Over the nearly 100 years since, our knowledge of galaxies has increased expo-

nentially. New telescopes and technologies have allowed us to analyze the light from galaxies to derive many of their properties, such as mass, luminosity, chemical make-up, star-formation rate, the rate of gas accretion onto the central supermassive black hole in the centre, and much more. Fortunately, the more we learn about them the more we realize just how much these structures can teach us about the evolution of the Universe from the beginning of time to the present day. Galaxies are excellent laboratories for studying physics on grand scales and testing theories of the true nature of the Universe.

Galaxies come in many different shapes and sizes. They can be generally divided into two broad categories: spirals and ellipticals. Spiral galaxies are arguably the most beautiful with their sweeping, gassy, blue spiral arms and disks. On the other hand, ellipticals tend to be round spheroids of stars mostly devoid of gas. Although perhaps less visually appealing than spirals, ellipticals represent the largest and smallest galaxies in the known Universe, ranging in mass from 10^7 to $10^{14}\,\mathrm{M}_\odot$. The highest mass giant elliptical galaxies are among the largest objects in the Universe, and are often found at the centres of galaxy clusters, while their lower mass "dwarf" elliptical counterparts are usually found either in isolation or orbiting other, larger galaxies and clusters. The faintest elliptical galaxies known to exist are called "dwarf spheroidal" (hereafter dSph) galaxies and have so far mainly been observed near the MW.

The MW belongs to a larger group of around 60 galaxies collectively called the Local Group. This group is dominated by two large spiral galaxies: the MW and Andromeda (M31). Nearly all of the other members are the much smaller dSph galaxies, many of which exist as satellites of either the MW or M31. Two satellites of the MW are so bright that they can be seen by the naked eye (but only from the Southern hemisphere): the Large and Small Megallanic Clouds (LMC and SMC, respectively). However, many of these satellite galaxies are so faint that they have only been discovered in the past few decades with the arrival of larger telescopes and innovative surveys. Indeed, with the recent Pan-Andromeda Archaeological Survey (PAndAS; McConnachie et al., 2009) and the Sloan Digital Sky Survey (SDSS; York et al., 2000), over 30 satellites have been discovered around M31, as well as roughly 25 thought to be associated with the MW (for an overview of their individual properties, see McConnachie, 2012). Most of these dSphs are devoid of gas, so information can only be gleaned from observations of their stars.

The MW dSphs can be classified into two luminosity regimes: "Ultrafaint" and "Classical". These two kinds of dSphs are defined as having an absolute V-band

magnitude, M_V, dimmer than or brighter than -8, respectively. This division makes reference to the Milky Way, where the "classical" satellite population is expected to be complete within the boundaries of the Galactic halo with the exception perhaps of the "zone of avoidance" created by dust absorption in the Galactic disc. "Ultra-faint" satellites, on the other hand, have only recently been discovered in Sloan Digital Sky Survey (SDSS) data. Their inventory is far from complete and their spatial distribution highly biased to relatively small nearby volumes in the region surveyed by SDSS (Koposov et al., 2008). As our technology improves, we will be able to probe to fainter and fainter magnitudes to detect more stars within the dSphs we have found, and to discover even more ultrafaints. For the majority of this thesis we shall restrict much of the comparison of our models with data on classical dSph systems.

Where do these galaxies come from? What do we know about their formation, and their evolution that brought them here to the present day? To answer these questions, we look toward cosmological models of structure formation in the Universe.

1.2 Cosmology

This is the way the Universe begins. Not with a whimper, but a bang. In 1929 Edwin Hubble observed that galaxies that are further away have their light spectra shifted toward longer, redder wavelengths (so-called "red-shifting"). The most popular interpretation of this phenomenon is that these galaxies are receding from us with a velocity proportional to their distance - a relation known as "Hubble's Law". It was this discovery that led astronomers to believe that the Universe is not static, but rather expanding all around us. This does not mean that we are in the centre of the Universe, that is how it would look from any point in space! If all of these galaxies are traced back in time, they can be found to originate from a common point in time when the Universe was extremely hot and dense - the Big Bang.

There are many models that attempt to explain how the Universe as we know it formed following the Big Bang. Most models assume the "cosmological principle", which states that, on large enough scales, the Universe is homogeneous (no location is special) and isotropic (it looks the same in all directions). This assumption is strongly supported by observations. The best-established theory is the Λ Cold Dark Matter (ΛCDM) cosmological model. In this model the matter in the Universe is today dominated by nonrelativistic (cold) matter that is dissipationless (does not radiate

and is thus "dark") and collisionless (interacts with itself and baryonic matter only through gravitation and possibly the weak interaction). Although the exact nature of this "dark matter" is unknown, its existence is needed to account for its gravitational influence on astronomical objects on a large range of scales – from the random stellar velocities in dwarf galaxies, to the rotation speeds of grand spiral galaxies, to the internal dynamics of galaxy clusters. Many projects are currently underway to directly and indirectly detect it, but so far no compelling evidence has been found. The rest of the matter in the Universe is baryonic (stars, gas, dust, atoms, humans, popsicles, etc), and accounts for only $\sim 15\%$ of its total matter content.

If the Universe were dominated only by matter, then its self-gravity would be expected to slow its expansion over time. However, through observations of supernovae in distant galaxies, it has been found that the Universe is not only expanding, but is accelerating in its expansion. This means that there must be some mysterious "dark energy" that makes up $\sim 70\%$ of the energy budget of the Universe and continues to drive the expansion faster and faster – this is the Λ term in ΛCDM.

ΛCDM has been extremely successful at describing our Universe today. It predicts very accurately all observations of the effects of the Big Bang, including the statistical structure of the cosmic microwave background (CMB), the abundances of light elements created via primordial nucleosynthesis, the accelerating expansion of the Universe, and the large-scale distribution of galaxies (Planck Collaboration et al., 2013; Steigman, 2007; Perlmutter et al., 1999; Eke, Cole & Frenk, 1996). Alternative theories include warm and hot (ie. relativistic) dark matter, self-interacting dark matter, and even modifications to current theories of gravity on galactic scales. Some of these theories have been somewhat more successful than ΛCDM at describing structure on small scales, although this subject is still under considerable debate (Colín, Valenzuela & Avila-Reese, 2008; Lovell et al., 2012; Macciò et al., 2013; Wang & White, 2009). Indeed such theories are not as extensive and developed as ΛCDM, and, in their current state, some make predictions that are inconsistent with observations (Viel et al., 2005). Because of the remarkable success and relative simplicity of ΛCDM, it has been widely accepted as the "standard" cosmological model of the Universe.

1.3 Simulations

One of the most powerful features of ΛCDM is its ability to predict the evolution of the matter distribution from the Big Bang to the present day. According to the model, the Universe is mostly smooth in the beginning except for small density fluctuations. Over time, regions of higher density collapse into spheroidal objects called haloes. The large scale structure of the Universe is then formed hierarchically through subsequent merging of these primordial haloes (Press & Schechter, 1974; Gott & Rees, 1975; White & Rees, 1978; Blumenthal et al., 1984). Indeed, by the present day many of these objects have disrupted and aggregated into larger objects, while others remain as substructures orbiting a larger host. The largest objects are generally dominated in mass by an extended dark matter halo, with the baryonic component sitting near the centre.

In the past couple of decades, cosmological N-body simulations have demonstrated how these structures form over time and have allowed us to compare this theory with observations (Tormen, 1997; Moore et al., 1999; Klypin et al., 1999a,b; Diemand et al., 2008; Springel et al., 2008; Stadel et al., 2009). Many of these simulations only include dark matter, neglecting the influence of baryonic matter. The main reason for this is that dark matter dominates baryonic matter 5:1 by mass and baryonic processes are only important on small scales, so for the large scale structure of the Universe, baryons play little role and tend to simply "follow" the dark matter through gravitation.

One recent example is the Millennium XXL simulation, which follows the evolution of 300 billion particles in a box of side length 4.1 Gpc over the entire 13.8 Gyr age of the Universe. A projected density plot from Angulo et al. (2012) is shown in Figure 1.1, which progressively zooms in on a halo of mass $10^{15}\,\mathrm{M}_{\odot}$, the most massive halo in the simulation. On the largest (Gpc) scales, this universe is homogeneous with no obvious features. As we zoom in to smaller (100 Mpc) scales, we see that matter forms long filamentary structures separated by large voids, often referred to as the "cosmic web". Matter flows along these filaments and forms large haloes at the intersecting nodes. In the third zoom-in panel, we begin to see a plethora of substructure accreting onto this halo. The internal structure of this halo is visible on the smallest scales shown, composed of the remains of disrupted primordial haloes.

Only recently have such cosmological simulations been able to adequately resolve substructures around Milky Way (MW)-sized dark matter haloes. They predict that

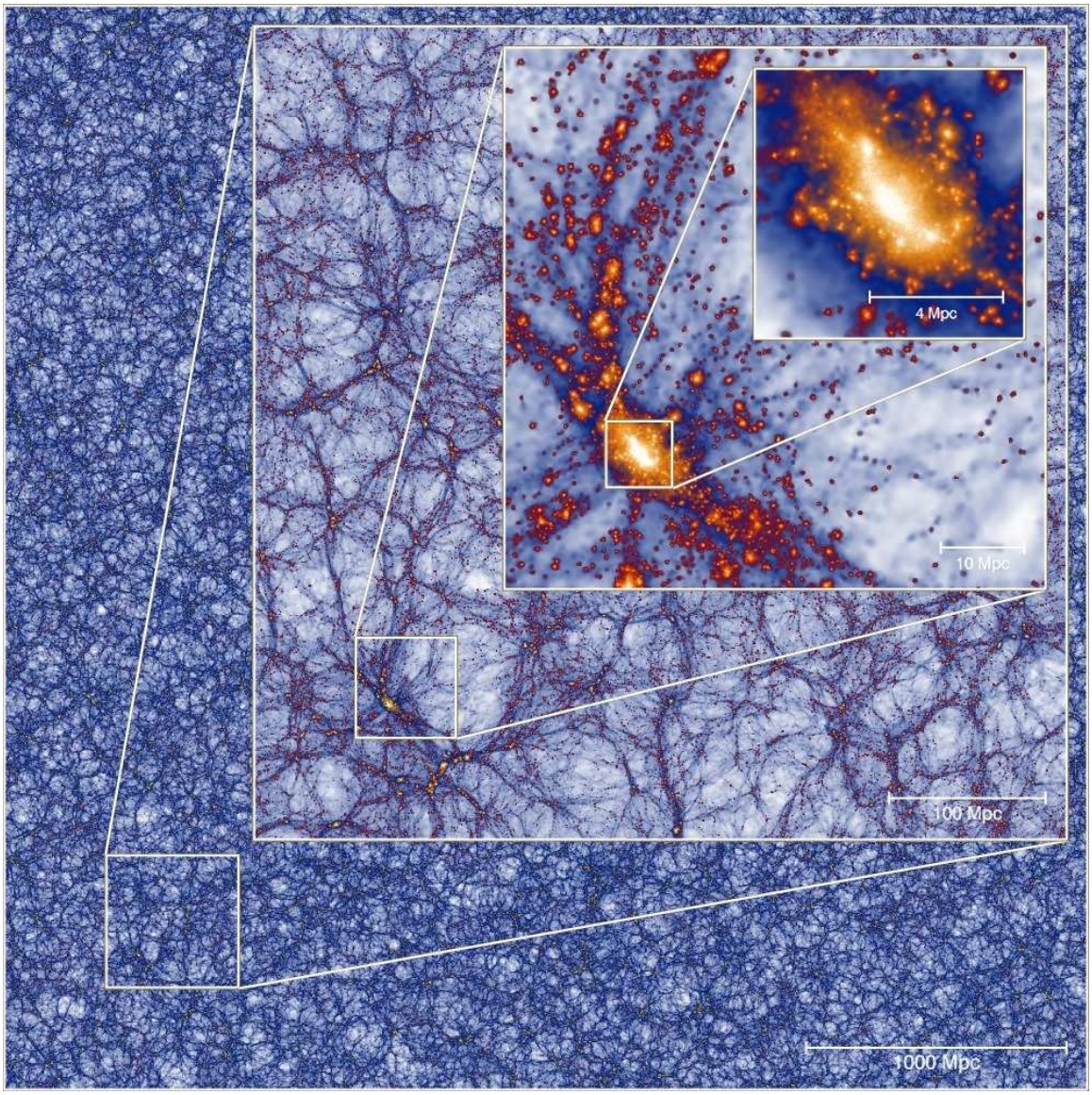

Figure 1.1: Projected density view of an 8 Mpc-thick slice of the Millennium XXL simulation at $z = 0$, progressively zooming into a halo of mass $10^{15}\,\mathrm{M}_{\odot}$. Figure taken from Angulo et al. (2012).

$\lesssim 20\%$ of the mass of such haloes is in the form of substructure haloes (hereafter subhaloes), which results in a very large number of satellites, most of which are extremely low mass (Springel et al., 2008). These subhaloes are particularly interesting because some of them are thought to host dSph galaxies similar to those found in our Local Group (Stoehr et al., 2002; Strigari et al., 2007; Boylan-Kolchin, Bullock & Kaplinghat, 2012a; Vera-Ciro et al., 2013; Starkenburg et al., 2013). Indeed, the dSphs in our Galactic "backyard" are thought to be the remnants of the hierarchical assembly of the MW, and thus give us a fossil record of its formation and subsequent evolution (Tolstoy, Hill & Tosi, 2009).

An important result of these dark matter-only simulations is the prediction that dark matter haloes tend to have a universal shape of their spherically-averaged radial density distributions (Navarro, Frenk & White, 1996, 1997). This "NFW" profile can be approximated as power laws at small and large radii, with a smooth transition between the two. For dark matter haloes this profile takes the form

$$\rho(r) = \frac{\rho_{\rm s}}{(r/r_{\rm s})(1 + r/r_{\rm s})^2} \tag{1.1}$$

where $\rho_{\rm s}$ and $r_{\rm s}$ are the characteristic density and radius of the halo, respectively. $\rho_{\rm s}$ is often expressed in terms of a concentration parameter c, defined as

$$\rho_{\rm s} = \rho_{\rm crit} \frac{200}{3} \frac{c^3}{\ln(1+c) - c/(1+c)}, \tag{1.2}$$

where $\rho_{\rm crit}$ is the critical density of the Universe for closure. The scale radius $r_{\rm s}$ is related to c via $r_{\rm s} = r_{200}/c$, where r_{200} is the virial radius of the halo. We define the virial radius as the radius within which the mean density of the halo is 200 times $\rho_{\rm crit}$. Although some profiles have been shown to be more accurate (eg. the Einasto profile, see Navarro et al., 2010), the NFW model has been widely used and is generally an excellent approximation to the density profile of galactic dark matter haloes in simulations.

Despite the many successes of ΛCDM, there remains some tension between theory and observation, especially on small scales. For instance, in simulations the central densities of dark matter haloes have been found to follow the NFW profile which is strongly cusped in the centre (Navarro, Frenk & White, 1996, 1997; Navarro et al., 2010; Fukushige & Makino, 1997; Moore et al., 1999; Diemand et al., 2008). On the other hand, some evidence shows that the dark matter haloes surrounding dwarf and

low surface brightness galaxies are likely to have flattened, "cored" central density profiles (Moore, 1994; Burkert, 1995; Gilmore et al., 2007; Walker & Peñarrubia, 2011), a discrepancy known as the "cusp-core" problem. Whether or not this is an issue for MW dSphs is currently under debate. Indeed, some recent studies argue that MW dSph observations may actually be consistent with cuspy dark matter profiles (Walker et al., 2009; Strigari, Frenk & White, 2010; Battaglia et al., 2011; Breddels et al., 2013).

Another conflict between ΛCDM models and observations on small scales is the "too big to fail" problem. Current theories of galaxy formation predict that dSph galaxies should form in the highest mass dark matter subhaloes. Boylan-Kolchin, Bullock & Kaplinghat (2011) found that, according to their simulations of MW-sized haloes, the most massive dark matter subhaloes are much more massive and dense than inferred from observations of MW dSphs. These massive subhaloes are theoretically "too big to fail" to accrete baryonic matter and form dSphs, and thus their presence in simulations presents a problem for the ΛCDM model. One possibility is that the number of massive satellites is a stochastic process and is highly sensitive to the mass of the host, a quantity currently only known within a factor of a few for the MW. Indeed, some authors argue that the "too big to fail" problem disappears for lower MW mass estimates (Wang et al., 2012; Vera-Ciro et al., 2013).

Also highly debated is the impact of baryonic processes on these small scales. During episodes of star formation in dSphs, the energy from supernova explosions may be strong enough to eject gas out from the centre of the halo. This outflow can cause the gravitational potential near the centre to change such that the dark matter cusp can be flattened out into a core, which may help to resolve the cusp-core problem (Navarro, Eke & Frenk, 1996; Read & Gilmore, 2005; Governato et al., 2010; Teyssier et al., 2013). In fact, it has been argued that the "too big to fail" problem may be solved by the fact that particles in cored haloes are less bound and thus may be more easily destroyed via tidal interactions with the host, especially in the higher mass haloes where baryonic effects are stronger. However, the importance of feedback on these scales is highly debated and it is still unclear whether the cusp to core transformation via stellar feedback is possible in MW dSphs, especially given their very low rates of star formation (Peñarrubia et al., 2012; Garrison-Kimmel et al., 2013).

The fact that the properties of galaxies on these small scales is so highly debated makes the study of dSphs very exciting. By attempting to match the predictions of

theoretical models with their observable properties, we can learn a plethora of information about galaxy formation and constrain cosmological models. It is particularly exciting because simulations that are detailed enough to resolve such small scales have only been possible within the past decade, meaning that we have only scratched the surface in terms of making robust predictions of dSphs in these simulations. In this thesis we use such simulations to make predictions for dSphs in the MW and compare with observations in order to learn about the dynamical histories of the MW dSphs; in doing so we constrain cosmological models in this small regime.

1.3.1 The Aquarius Project

The Millennium II simulation is a dark-matter only cosmological simulation of a cubic region of the Universe $100h^{-1}$Mpc on a side using 10 billion dark matter particles. The simulation we use in this thesis, entitled the Aquarius Project, is a resimulation of six MW-sized dark matter haloes taken from Millennium II, run at higher resolution. A zoom-in technique was used in which particles that end up inside or near the main halo are resimulated at higher resolution (more particles each with lower mass), while those outside are given lower mass resolution. These haloes, named Aq-A through Aq-F, range in virial mass M_{200} from $(0.8 - 1.8) \times 10^{12}\,\mathrm{M}_\odot$, which is the typical range of the latest estimates of the MW's virial mass. The haloes were simulated at various resolution levels, denoted with a suffix from 1 to 5. The Aq-A halo has been simulated at all five resolution levels; the highest resolution run (Aq-A-1) has over 4 billion high-resolution particles, a particle mass of $2 \times 10^3\,\mathrm{M}_\odot$ and a softening length of 20 pc. The other five haloes were simulated at intermediate (level 2 and 4) resolution, with particle mass $\sim 10^4$ and $2 \times 10^5\,\mathrm{M}_\odot$ respectively. The main properties of the Aquarius haloes used in this thesis are shown in Table 1.1. Here we show the high-resolution particle mass, gravitational softening parameter, number of high and low resolution particles, virial mass and radius, NFW concentration parameter, and the redshift of halo formation. The halo formation time is defined as the epoch at which the virial mass of the halo was half of its final value. All parameters shown here are taken directly from Springel et al. (2008). A projected density plot of the Aq-A-2 main halo is shown in Figure 1.2. At this resolution level, subhaloes can be resolved down to $10^5\,\mathrm{M}_\odot$. Considering that MW dSphs typically have masses of $\sim 10^7\,\mathrm{M}_\odot$ within 300 pc (Strigari et al., 2008), the Level-2 resolution level is sufficient to resolve and study dark matter haloes that are likely to host galaxies similar to the

MW dSphs in detail.

Table 1.1: Basic parameters of the Aquarius simulations (Springel et al., 2008).

Name	$m_{\rm p}$ ($M_\odot$)	ϵ (pc)	$N_{\rm hr}$	$N_{\rm lr}$	M_{200} ($M_\odot$)	r_{200} (kpc)	$c_{\rm NFW}$	$z_{\rm form}$
Aq-A-1	1.712×10^3	20.5	4 252 607 000	144 979 154	1.839×10^{12}	245.76	16.11	1.93
Aq-A-2	1.370×10^4	65.8	531 570 000	75 296 170	1.842×10^{12}	245.88	16.19	1.93
Aq-A-3	4.911×10^4	120.5	148 285 000	20 035 279	1.836×10^{12}	245.64	16.35	1.93
Aq-A-4	3.929×10^5	342.5	18 535 972	634 793	1.838×10^{12}	245.70	16.21	1.93
Aq-A-5	3.143×10^6	684.9	2 316 893	634 793	1.853×10^{12}	246.37	16.04	1.93
Aq-B-2	6.447×10^3	65.8	658 815 010	80 487 598	8.194×10^{11}	187.70	9.72	1.39
Aq-C-2	1.399×10^4	65.8	612 602 795	78 634 854	1.774×10^{12}	242.82	15.21	2.23
Aq-D-2	1.397×10^4	65.8	391 881 102	79 615 274	1.774×10^{12}	242.85	9.37	1.51
Aq-E-2	9.593×10^3	65.8	465 905 916	74 119 996	1.185×10^{12}	212.28	8.26	2.26
Aq-F-2	6.776×10^3	65.8	414 336 000	712 839	1.135×10^{12}	209.21	9.79	0.55

Haloes are identified in the simulation using a standard friends-of-friends (FOF) technique (Davis et al., 1985). Substructures within haloes are subsequently identified by locating overdensities within the average background density field using the groupfinder SUBFIND (Springel et al., 2005). This algorithm recursively identifies all self-bound substructures that contain at least 20 particles.

The Aquarius simulations assume a "standard" ΛCDM cosmogony, with the same parameters as the Millennium Simulation (Springel et al., 2005): $\Omega_{\rm M} = 0.25$, $\Omega_\Lambda = 0.75$, $n = 1$, $h = 0.73$, and $\sigma_8 = 0.9$. Although the exact values used for these parameters are now outdated considering the recently published results from the Planck satellite (Planck Collaboration et al., 2013), we expect the difference to have little effect on the detailed non-linear structure and substructure of dark matter haloes which concern us here (see, e.g., Wang et al., 2008; Boylan-Kolchin et al., 2010; Guo et al., 2013).

1.3.2 The semi-analytic model

In order to properly study dSphs in simulations, we must be able to follow the baryonic matter that makes up these galaxies through time. One approach is to explicitly include "gas" particles in the simulation along with the dark matter and solve the hydrodynamical equations that govern its evolution. Unfortunately, this approach is much more computationally expensive than the purely N-body dark matter simulations. Thus, rather than simulating the baryons directly, often a semi-analytic

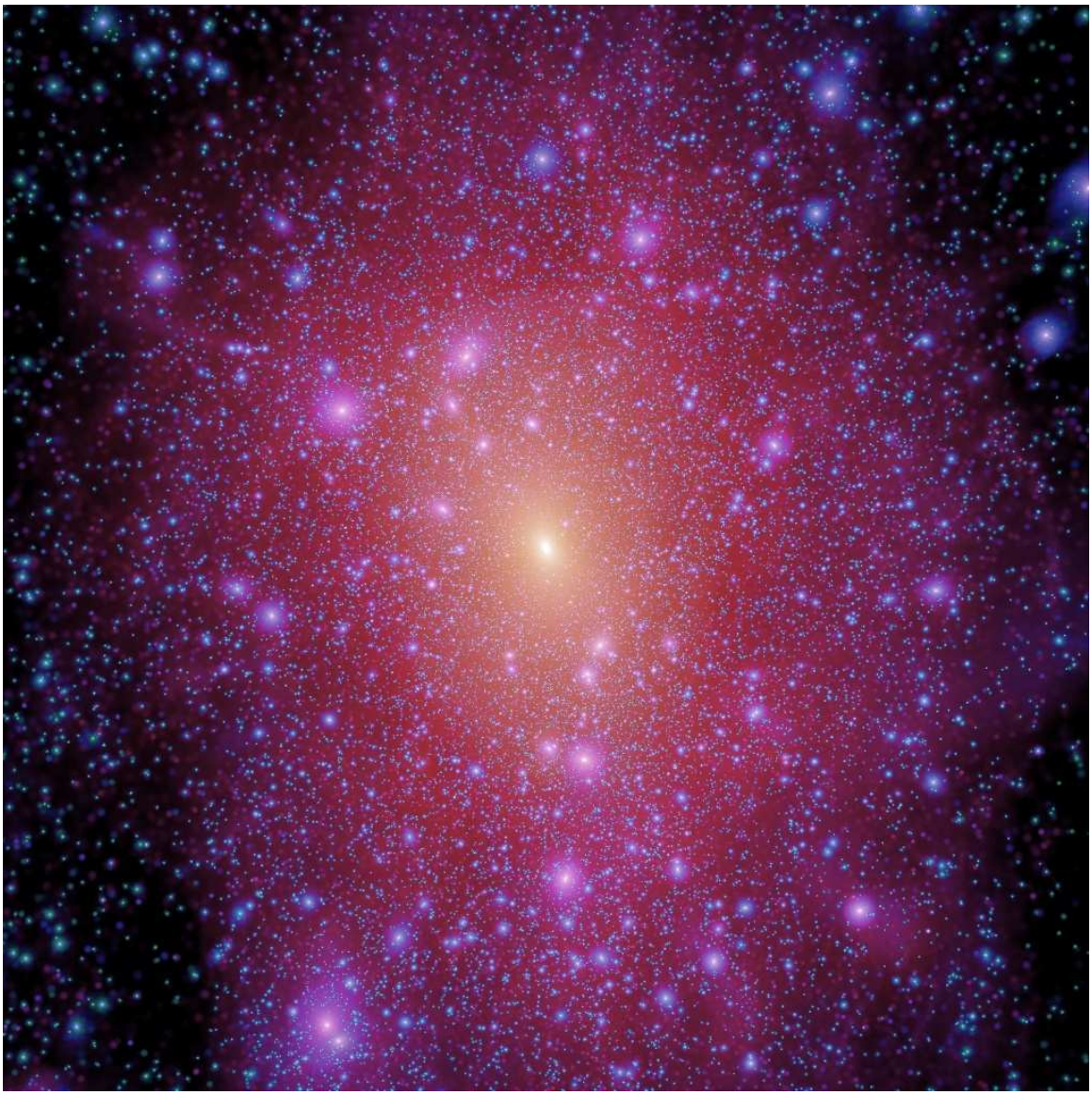

Figure 1.2: Projected density plot centred on the main halo of Aq-A-2. All particles within a box of side length 1 Mpc are shown. Figure taken from Springel et al. (2008).

model is implemented after the dark matter simulation has been run. These models use the dark matter distribution as a backbone for the overall distribution of matter over time. Here one employs simple, observationally motivated equations to model the underlying baryonic processes expected to occur in the Universe. In this way, one can estimate the properties of galaxies expected to reside within the dark matter haloes. This method is much more computationally efficient and thus allows a more thorough exploration of the input parameters and assumptions than can be done in full hydrodynamical simulations. The downside to this method is that one recovers only global properties of the baryonic matter in each halo, in contrast with the full structural information that can be obtained in hydrodynamical simulations. As well, any impact that the baryons may have on the dark matter distribution is ignored. However, the strength of such impact is highly debated, especially on the scales of the dark matter-dominated dwarf galaxies (Peñarrubia et al., 2012; Garrison-Kimmel et al., 2013).

In this thesis we consider a semi-analytic model of galaxy formation in order to identify which dark matter subhaloes in Aquarius are most likely to contain dSphs like those found in the Local Group. This model is grafted onto the evolving collection of SUBFIND haloes and subhaloes linked as a function of time by a merger tree (Baugh, 2006; Benson, 2010). The particular implementation used in this thesis is described by Starkenburg et al. (2013) and is an extension of earlier work (Kauffmann et al., 1999; Springel et al., 2001; De Lucia, Kauffmann & White, 2004; Croton et al., 2006; De Lucia & Blaizot, 2007; De Lucia & Helmi, 2008; Li et al., 2009; Li, De Lucia & Helmi, 2010). Included in the model are analytic prescriptions for the reionization of the early Universe, star formation in regions of high gas density, gas cooling, and heating and ejection of hot gas due to supernova feedback. Interactions between satellite galaxies and their host are also included in the form of tidal disruption and stellar stripping, as well as ram-pressure stripping of hot gas from the satellite after infall. This model has been very successful at matching the observed luminosity function, luminosity-metallicity relation, and radial distribution of the MW dSph galaxies, and results in a halo mass-stellar mass relation that is in agreement with full hydrodynamical simulations.

1.4 This Thesis

Armed with the Aquarius Project and our semi-analytic model, in this thesis we study the properties of the haloes of dSph galaxies around MW-sized haloes as predicted by ΛCDM. In doing so, we are able to make robust predictions of MW dSphs that can be compared directly with observations.

In Chapter 2, we analyze the orbital properties of dSph satellites in the Aquarius haloes. By comparing these orbits with those of subhaloes that did not form dSphs, we obtain valuable insight into how these satellites evolve over time after accreting into the main halo. We also present a novel technique for estimating the mass of the MW by comparing the orbits of the brightest simulated galaxies with the positions and velocities of the MW dSphs. As observations continue to improve, this technique should prove quite valuable at providing a stricter value for the MW's mass.

In Chapter 3, we measure the shapes and orientations of the Aquarius dSph satellites. In doing so, we make robust predictions about the impact of the host tidal field on its satellites, and describe how observations of the shapes and orientations of satellite galaxies can inform us about their dynamical histories.

In Chapter 4 we provide a summary and conclusions, as well as an outline of possible extensions of this work in the future.

Chapter 2

The Orbital Ellipticity of Satellite Galaxies and the Mass of the Milky Way[1]

[1]Based on Barber C., Starkenburg E., Navarro J. F., McConnachie A. W., Fattahi A., 2014, MNRAS, 437, 959

Abstract

We use simulations of Milky Way-sized dark matter haloes from the Aquarius Project to investigate the orbits of substructure haloes (subhaloes) likely, according to a semi-analytic galaxy formation model, to host luminous satellites. These tend to populate the most massive subhaloes and are on more radial orbits than the majority of subhaloes found within the halo virial radius. One reason for this (mild) kinematic bias is that many low-mass subhaloes have apocentres that exceed the virial radius of the main host; they are thus excluded from subhalo samples identified within the virial boundary, reducing the number of subhaloes on radial orbits. Two other factors contributing to the difference in orbital shape between dark and luminous subhaloes are their dynamical evolution after infall, which affects more markedly low-mass (dark) subhaloes, and a weak dependence of ellipticity on the redshift of first infall. The ellipticity distribution of luminous satellites exhibits little halo-to-halo scatter and it may therefore be compared fruitfully with that of Milky Way satellites. Since the latter depends sensitively on the total mass of the Milky Way we can use the predicted distribution of satellite ellipticities to place constraints on this important parameter. Using the latest estimates of position and velocity of dwarfs compiled from the literature, we find that the most likely Milky Way mass lies in the range $6 \times 10^{11}\, M_\odot < M_{200} < 3.1 \times 10^{12}\, M_\odot$, with a best-fit value of $M_{200} = 1.1 \times 10^{12} M_\odot$. This value is consistent with Milky Way mass estimates based on dynamical tracers or the timing argument.

2.1 Introduction

Satellite galaxies have long been used as kinematic tracers of the gravitational potential of the Milky Way (MW) halo (e.g., Hartwick & Sargent, 1978; Lynden-Bell, Cannon & Godwin, 1983; Zaritsky et al., 1989; Kulessa & Lynden-Bell, 1992; Kochanek, 1996; Wilkinson & Evans, 1999; Battaglia et al., 2005; Sales et al., 2007a; Boylan-Kolchin et al., 2013). The usefulness of this technique, however, has been traditionally limited by the relatively small number of satellites known, by uncertainties in their estimated distances, and by the availability of a single component of the orbital velocity, along the line of sight. This state of affairs, however, is starting to change.

Over the last decade, surveys like the Sloan Digital Sky Survey (SDSS) have mapped large areas of the sky, an effort that has led to the discovery of a number of very faint satellite galaxies (the "ultra-faint" dwarf spheroidal companions of the Milky Way) whose star formation history, chemical evolution, mass, distance, and velocity have now been estimated through deep follow-up observations (e.g., Willman et al., 2005; Zucker et al., 2006a,b; Belokurov et al., 2007; Walsh, Jerjen & Willman, 2007; Irwin et al., 2007; Kirby et al., 2008; Martin, de Jong & Rix, 2008; Adén et al., 2009; Norris et al., 2010; Wolf et al., 2010; Simon et al., 2011; Brown et al., 2012). Distance estimates have also improved, to the point that the distances to most satellites are now known to better than $\sim 10\%$ from measurements of resolved stellar populations. Further, the superior angular resolution of the Hubble Space Telescope has enabled proper motion estimates for nearby dwarfs from images with a time baseline of just a few years (e.g., Piatek et al., 2002), and modern adaptive optics systems promise to reach comparable angular resolution from the ground (e.g., Rigaut et al., 2012). Finally, in the near future, a great leap forward is expected from the Global Astrometry Interferometer for Astrophysics (Gaia) satellite (e.g., Lindegren & Perryman, 1996). This mission is expected to measure the proper motions of the MW dwarf spheroidal system to an precision of a few to tens of $\mathrm{km\,s^{-1}}$, depending on the satellite's properties (Wilkinson & Evans, 1999).

Accurate proper motions, radial velocities, positions, and distances can be turned into satellite orbits after assuming a mass profile for the Galaxy. The shapes of these orbits are expected to contain information about the circumstances of the accretion of individual satellites, as well as about the evolution of the potential well of the Galaxy over time. Decoding such information, however, is not straightforward, and is best attempted by contrasting observations with realistic simulations that resolve

in detail the dynamical evolution of the potential sites of dwarf galaxy formation.

Although there are in the literature a number of studies of the kinematics of satellite systems and their relation to the haloes they inhabit (e.g., Tormen, 1997; Tormen, Diaferio & Syer, 1998; Ghigna et al., 1998; van den Bosch et al., 1999; Balogh, Navarro & Morris, 2000; Taffoni et al., 2003; Kravtsov, Gnedin & Klypin, 2004; Gill et al., 2004; Gill, Knebe & Gibson, 2005; Diemand, Kuhlen & Madau, 2007; Sales et al., 2007a; Ludlow et al., 2009), most have dealt primarily with the orbits of substructure haloes (referred to hereafter as subhaloes) in general. Luminous satellites inhabit a small fraction of subhaloes, and their orbits might therefore very well be substantially biased relative to those of typical subhaloes. Making progress demands not only simulations with numerical resolution high enough to resolve all potential sites of luminous satellite formation but also a convincing way of pinpointing the few subhaloes where those satellites actually form.

A number of simulations that satisfy the numerical resolution requirement have been recently completed, notably the six Milky Way-sized haloes of the Aquarius Project (Springel et al., 2008), as well as the Via Lactea II halo (Diemand et al., 2008), and its higher-resolution version GHALO (Stadel et al., 2009). In this study we combine the Aquarius Project haloes with the semi-analytical model of Starkenburg et al. (2013) to identify satellites with luminosities down to the "ultra-faint" regime. We study the orbital distribution of these satellites, and explore its dependence on satellite properties such as stellar mass and accretion time. Our analysis yields predictions that should prove useful in the near future, when Gaia delivers accurate 6D phase space information for many Milky Way satellites. We describe here a possible application, making use of published proper motions, positions and radial velocities of the most luminous Milky Way satellites to constrain the mass of the Milky Way halo.

The plan of this chapter is as follows. In Section 2.2 we describe the simulated satellite sample we use, together with a brief discussion of the numerical simulations and of the semi-analytic galaxy formation model adopted. We describe the analysis techniques used to compute orbital properties for satellites and subhaloes and present their orbital ellipticity distributions in Section 2.3. We investigate in the same section the origin of their differences before, finally, in Section 2.4, comparing the orbits of simulated dwarf galaxies to those of MW dwarfs in order to discuss the constraints they imply on the total virial mass of the Milky Way. We summarize our main conclusions in Section 2.5.

2.2 Simulated Satellites

As discussed in Chapter 1, we use the Aquarius project, a cosmological dark matter-only simulation of six MW-sized haloes, to study the substructure of MW-like galaxies. Coupled with the semi-analytic model of Starkenburg et al. (2013), we are able to identify those subhaloes that are most likely to contain a luminous component, had baryons been included in the simulation.

The semi-analytic model assigns a stellar mass (or luminosity) to each subhalo at the present time. We classify them as: (i) "classical" satellites (i.e., those brighter than $M_V = -8$); (ii) "ultra-faint" satellites (fainter than $M_V = -8$); and (iii) "dark" subhaloes (i.e., those with no stars). We shall hereafter use the term "luminous subhaloes" to refer to classical and ultra-faint satellites combined.

2.3 Analysis and Results

2.3.1 Satellite masses and radial distribution

As discussed by Starkenburg et al. (2013), the simulated satellite luminosity function of Aquarius haloes is consistent with that of the Milky Way. Luminous satellites populate a minority of the subhalo population, preferentially the high-mass end. Indeed, by number, most subhaloes have low mass and, according to the model, remain completely "dark" throughout their lifetime.

Figure 2.1 shows the mass distribution of all subhaloes identified at $z = 0$ *within the virial radius*, r_{200}, of each of the six Aquarius haloes considered here. Masses are quoted at the time of first infall into the main progenitor of each halo ($t_{\rm inf}$), and correspond roughly to the maximum virial mass of each subhalo prior to accretion. We also show in Figure 2.1 the subhalo masses of the luminous satellites and confirm that, as expected, they tend to populate the most massive subhaloes.

Low-mass subhaloes clearly dominate the numbers down to $10^6\,M_\odot$, where the distribution peaks. The decline in numbers at lower masses results from limited numerical resolution (see Springel et al., 2008, for a detailed discussion). We shall therefore consider for analysis only subhaloes with virial mass exceeding $10^6\,M_\odot$ at first infall, or haloes with more than ~ 100 particles. Combining all six simulations, our full satellite sample consists of $50,874$ subhaloes, of which 452 host luminous satellites: 296 ultra-faint and 156 classical dwarfs, respectively.

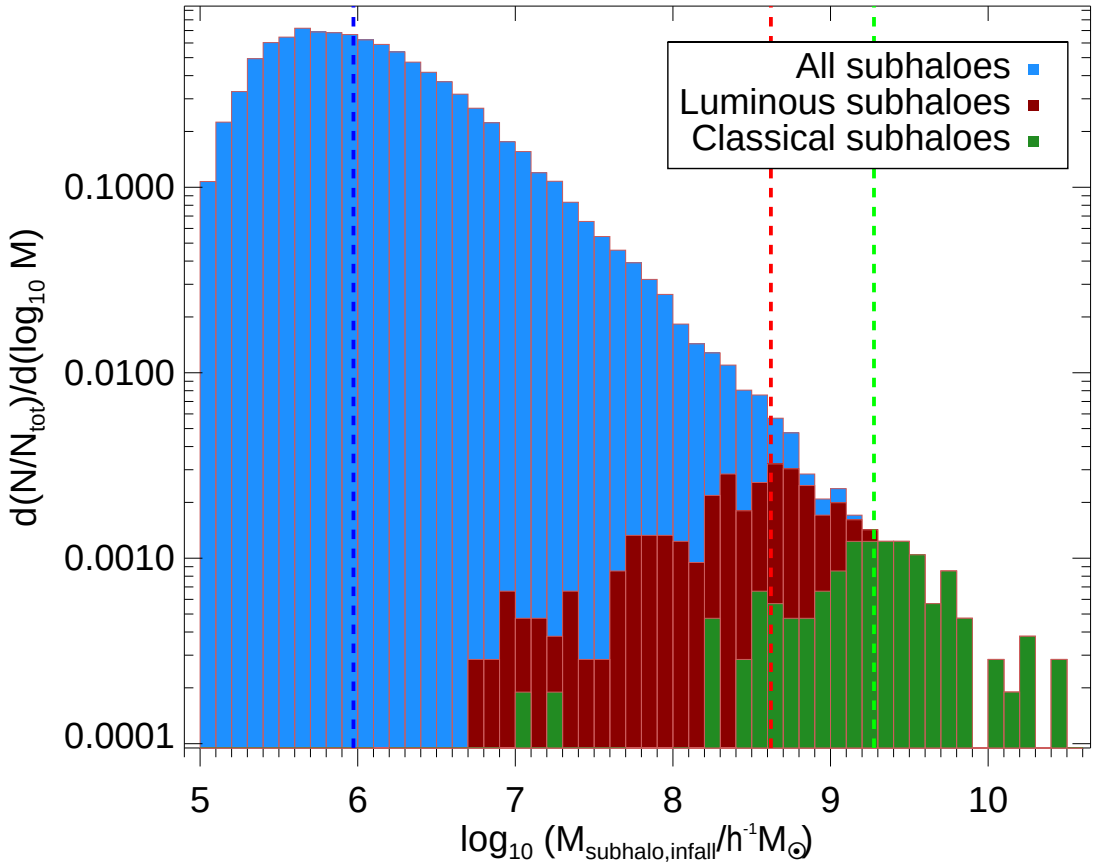

Figure 2.1: Mass distribution of subhaloes found, at $z = 0$, within the virial radius, r_{200}, of the level-2 Aquarius A through F haloes. Their (virial) masses are computed at the time of first infall into the main progenitor of the main halo. All subhaloes are shown in blue, luminous satellites in red, and classical satellites in green. Vertical dashed lines indicate the median of each group. Luminous satellites populate preferentially the high-mass end of the subhalo mass function. The decline in numbers below $\sim 10^6\, h^{-1}\, M_\odot$ results from limited numerical resolution. We consider only subhaloes with masses exceeding $\sim 10^6\, h^{-1}\, M_\odot$ in our subsequent analysis.

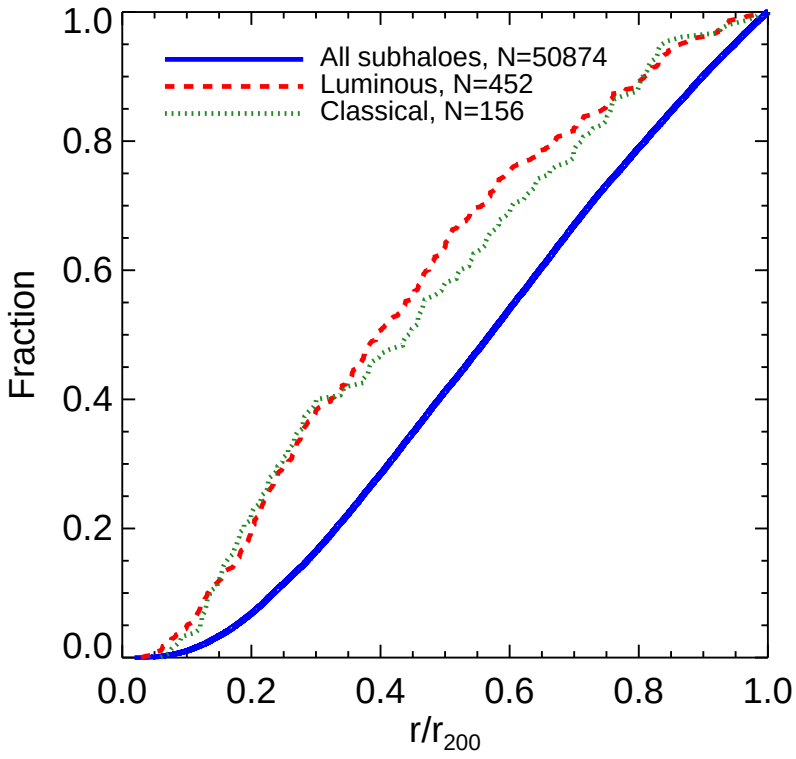

Figure 2.2: Fraction of enclosed subhaloes as a function of radius for level-2 Aquarius haloes A through F. All subhaloes are shown as a blue solid line; the subset of luminous satellites as a red dashed line, and only the classical as a green dotted line.

Figure 2.2 shows the radial distribution of the three populations of subhaloes in our model. Luminous satellites are noticeably more centrally concentrated than the majority of subhaloes (e.g., Gao et al., 2004; Starkenburg et al., 2013), a bias that might affect the comparison between the orbital properties of luminous and dark subhaloes. Another noticeable difference between the luminous and non-luminous subhalo population is the distribution of their infall times, $t_{\rm inf}$. As shown in Figure 2.3, the luminous subhaloes tend to fall in earlier.

2.3.2 Orbital ellipticity distributions

We compute the ellipticity, e, of the orbit of each subhalo from its current apocentric, r_a, and pericentric, r_p, distances,

$$e \equiv \frac{r_a - r_p}{r_a + r_p}, \tag{2.1}$$

using the virial mass and concentration of the main halo. The calculation assumes that the halo mass profile follows the NFW (NFW, Navarro, Frenk & White, 1996, 1997) formula, where the gravitational potential is written as

$$\Phi(r) = -4\pi G \rho_s r_s^2 \, \frac{\ln\left(1 + r/r_s\right)}{r/r_s}. \tag{2.2}$$

Here r is the distance from the centre of the main halo, and r_s and ρ_s are the NFW scale radius and density, respectively. The scale radius, r_s, is related to the halo concentration by $r_s = r_{200}/c$, where c is the NFW concentration parameter. The scale density, on the other hand, is related to the concentration parameter by

$$\frac{\rho_s}{\rho_{\rm crit}} = \frac{200}{3} \, \frac{c^3}{\ln(1+c) - c/(1+c)}. \tag{2.3}$$

The ellipticity distributions of the three subhalo populations at $z = 0$ are shown in Figure 2.4. The orbits of luminous satellites are clearly more radial than those of the subhalo population as a whole, which is dominated by the numerous low-mass, "dark" systems. Half of all subhaloes are on orbits with $e < 0.59$, but the median e is significantly larger for luminous systems: 0.68 for all luminous and 0.65 for classical satellites. As indicated by a Kolmogorov-Smirnov (KS) test, the distributions are very significantly different indeed. (The probability that the e-distribution of each satellite

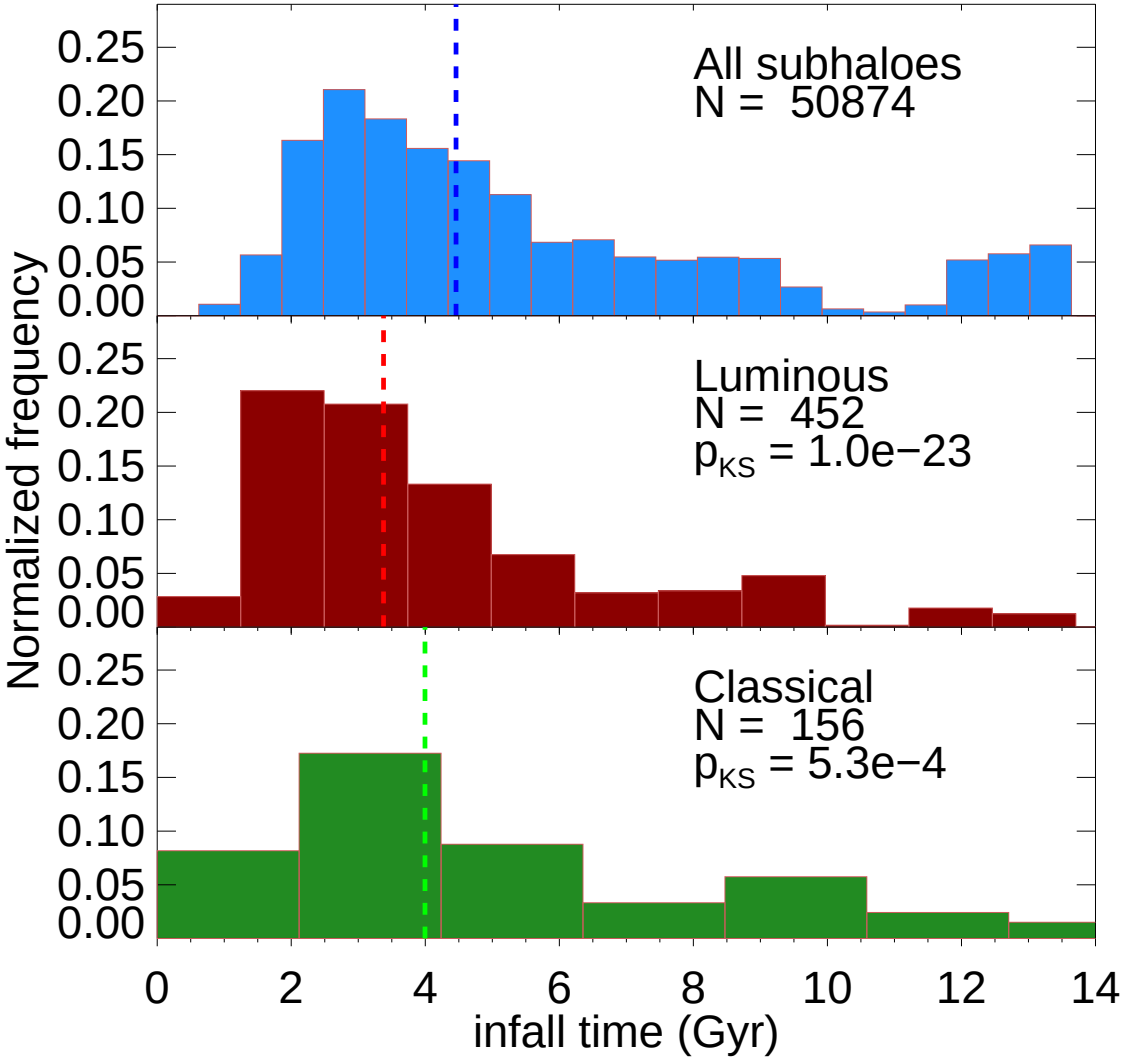

Figure 2.3: Distribution of first-infall cosmic times (where zero corresponds to the Big Bang) for satellites identified within the virial radius of the main halo at $z = 0$. Medians are indicated by vertical dashed lines. The normalization of the frequency is chosen such that the area under each histogram equals unity. Luminous (i.e., ultra-faint and classical) satellites enter the most massive progenitor of the main halo earlier than the average subhalo. N indicates the number of subhaloes in each grouping. KS tests indicate the probability that the luminous or classical samples are drawn from the same parent population as all subhaloes.

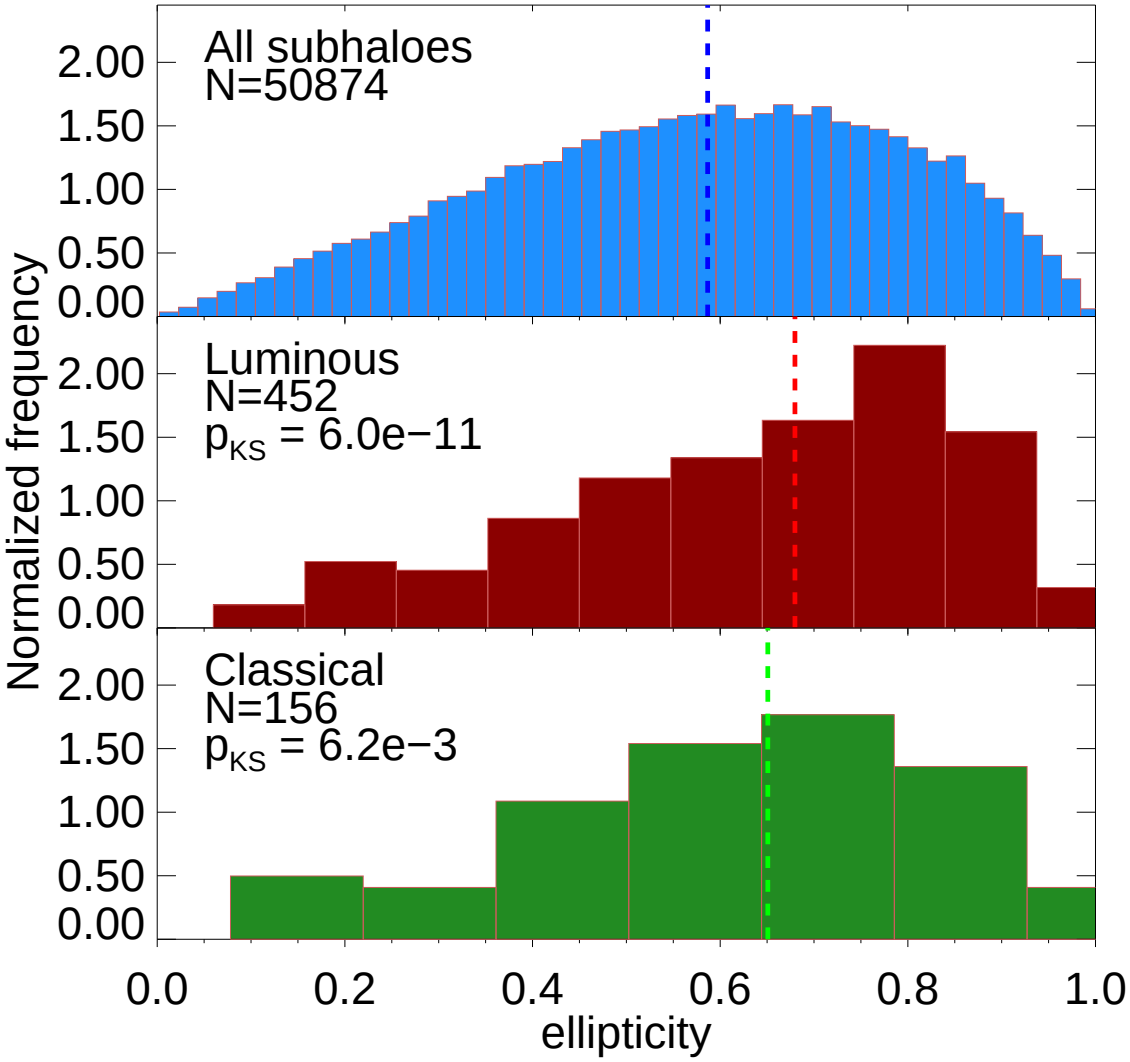

Figure 2.4: As in Figure 2.3, but for the ellipticity distributions of all subhaloes (top); all luminous (middle); and just the classical dwarfs (bottom), measured at $z = 0$. Medians are indicated by vertical dashed lines. KS tests indicate the probability that the observed luminous and classical satellite ellipticities are drawn from the same parent population as that of all subhaloes.

grouping is drawn from the same parent distribution as all subhaloes is listed in the middle and bottom panels.) This result is in qualitative agreement with pioneering work from Tormen (1997) who found that within simulated cluster environments more massive satellites move along more eccentric orbits than lower mass satellites.

Classical satellites are on slightly less radial orbits than ultra-faints (as is reflected in the higher median e for all luminous subhaloes, compared to just the classical satellite subset), but the difference between the two has lower significance; a KS test yields a p-value of 0.65.

We note that our modelling neglects the effect of baryons and, in particular, of the potential modifications that the presence of a massive stellar disc may have on the subhalo mass function and their orbits. A recent study by D'Onghia et al. (2010), for example, shows that disc shocking may be able to destroy preferentially low-mass subhaloes on plunging orbits. This would presumably skew their ellipticity distribution to less radial orbits and would enhance the differences noted above between the ellipticity distributions of "dark" and "luminous" satellites.

2.3.3 Radial selection biases and dynamical evolution

What is the origin of the systematic differences in the orbital shapes of luminous and dark subhaloes?

A clue is provided by the distribution of infall times of all subhaloes. As seen in the top panel of Figure 2.3, a notable feature is that there is a well-defined dip in the number of satellites with $t_{\rm inf}$ of the order of ~ 11 Gyr, followed by a sharp upturn a couple of Gyr later. We have verified that the dip is actually present in all Aquarius haloes taken individually, and does not reflect a particular event in the accretion history of individual haloes.

Rather, the dip may be traced to the fact that many subhaloes accreted at $t_{\rm inf} \sim 11$ Gyr are found temporarily outside the virial boundary of the halo at $z = 0$. Indeed, the radial period of an object released at rest from the virial radius is roughly ~ 3 Gyr; most systems accreted at $t_{\rm inf} \sim 11$ Gyr have apocentric radii that exceed r_{200}, and the majority of them are today therefore beyond the formal virial boundary of the halo. As discussed in detail by Ludlow et al. (2009) (see also Balogh, Navarro & Morris, 2000; Mamon et al., 2004; Gill, Knebe & Gibson, 2005; Diemand, Kuhlen & Madau, 2007; Ludlow et al., 2009; Wang, Mo & Jing, 2009), subhaloes identified within the virial radius represent a rather incomplete census of the substructure phys-

ically related to a halo: many "associated[2]" subhaloes are found outside the formal virial radius of a halo at any given time. The effect is mass-dependent: associated subhaloes outside r_{200} tend to be preferentially low mass.

We show this explicitly in Figure 2.5, where we compare the apocentric radii of all associated subhaloes with those of luminous ones. Selecting systems within r_{200} includes more than 80% of all luminous associated satellites, but leaves out nearly half of the less massive, dark subhaloes. This introduces a substantial bias in the apocentric radii of the latter, selecting preferentially systems with smaller apocentres. The effect on the orbital ellipticity distribution is to favour systems with less radial orbits.

This may be seen in Figure 2.6, where we compare the ellipticity distributions of various samples of luminous and dark subhaloes. The top two panels show that the dark and luminous subhalo ellipticity distributions become more similar when considering all associated subhaloes rather than selecting only those within r_{200}. The radial selection bias, however, is not enough to explain the systematic difference between the two populations, as shown by the low probability of a KS test (see legends in each panel of Figure 2.6).

The remaining difference is due partly to the fact that the orbits of dark and luminous subhaloes evolve differently after being accreted into the main halo. This is shown in the third panel of Figure 2.6, where ellipticities measured at the time of first infall are compared. Although still significantly different, ellipticities of associated dark and luminous subhaloes are much closer at infall than at $z = 0$.

The top three panels of Figure 2.6 also indicate that it is mainly the ellipticities of low-mass (dark) subhaloes that change appreciably after infall: their orbits tend to become less radial with time, something that is not seen in the luminous satellites. Possible scenarios for this "circularization" of low-mass subhaloes include the tidal dissolution of the groups to which they belong at accretion, but also perturbations by massive subhaloes they encounter on their orbits within the host halo (e.g., Tormen, Diaferio & Syer, 1998; Taffoni et al., 2003). We have explicitly checked that this conclusion is not the result of limited numerical resolution: we obtain similar results even if we raise the minimum subhalo mass considered in our sample from $10^6 M_\odot$ to $10^7 M_\odot$, or even $10^8 M_\odot$.

[2]We denote as "associated" all subhaloes that survive to $z = 0$ and were, at any time during their evolution, within the (evolving) virial radius of the main halo. The number of associated subhaloes nearly doubles the number within the virial radius: we identify 89,079 associated subhaloes in all six level-2 Aquarius haloes combined.

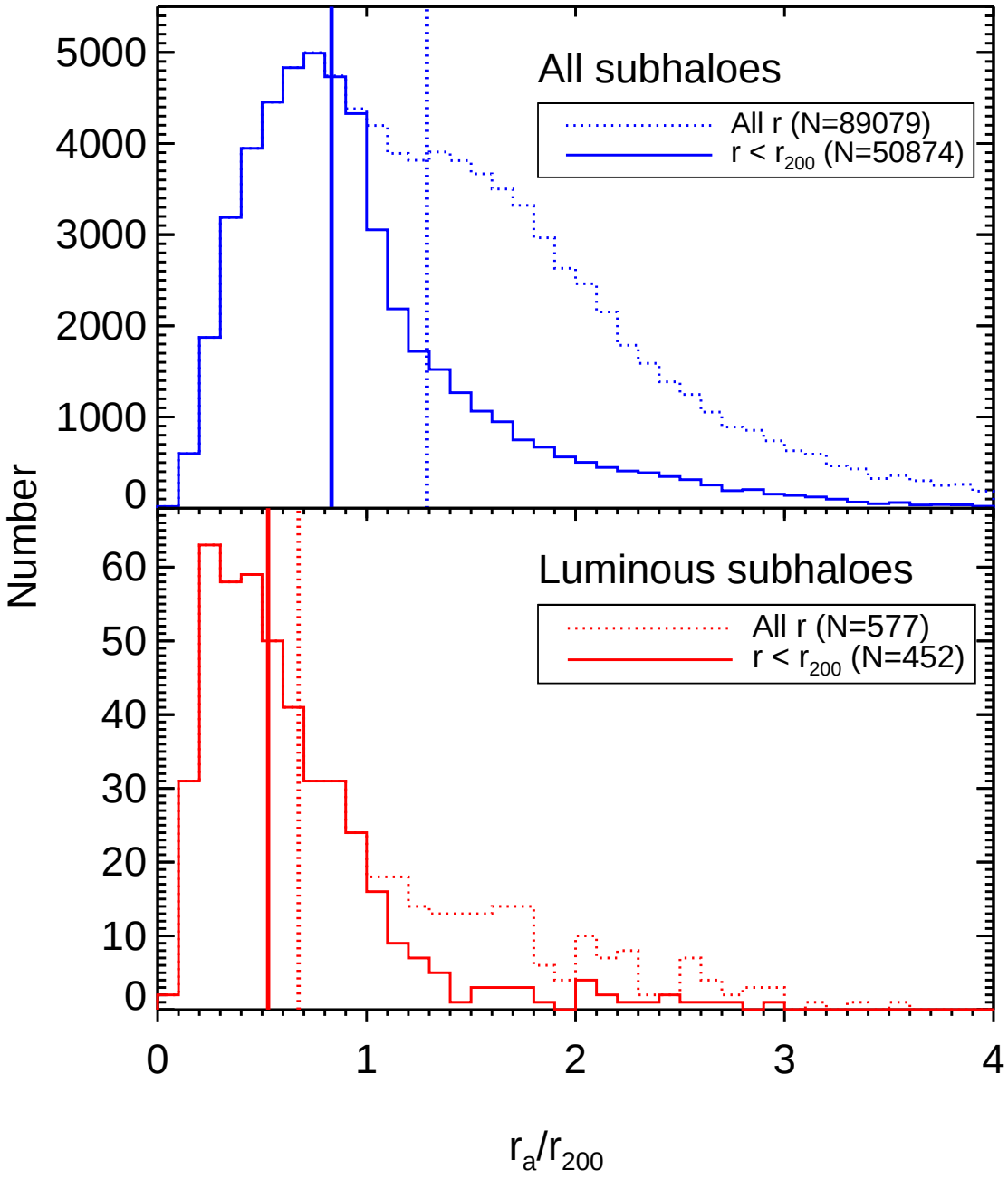

Figure 2.5: Distribution of apocentric radii for all subhaloes and luminous subhaloes (top and bottom panels, respectively). Solid lines correspond to subhaloes found within r_{200} at $z = 0$; dotted lines to all "associated" subhaloes. Note that few ($\sim 20\%$) luminous subhaloes are found outside the virial radius; on the other hand, selecting only systems within the virial radius excludes nearly half of all (mostly low-mass) associated subhaloes.

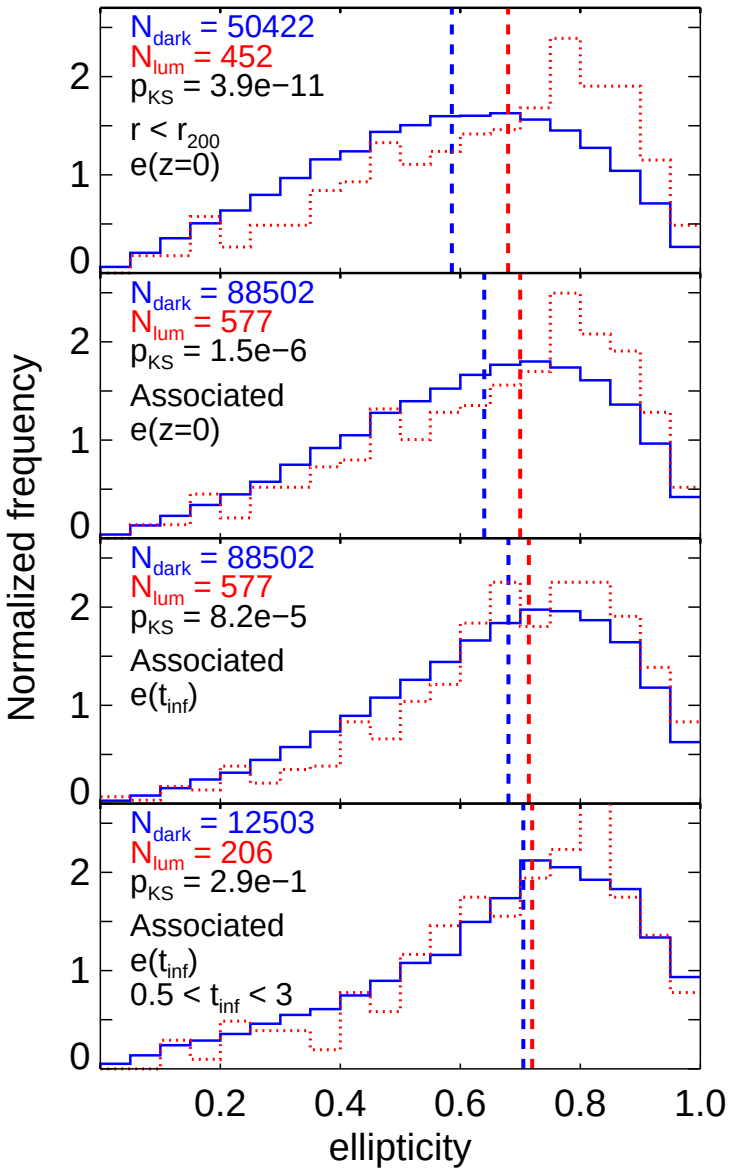

Figure 2.6: Ellipticity distributions of luminous and non-luminous subhaloes (red dotted and blue solid lines respectively). Medians are indicated by vertical dashed lines. The listed p-values in each panel correspond to the KS test between the luminous and non-luminous subhalo distributions shown in that panel. The normalization is chosen such that the area under each curve is unity. *Top panel:* only subhaloes with $r < r_{200}$ are considered, their ellipticity distributions are measured at $z = 0$. *Second panel:* Same as in the top panel, but including all "associated" subhaloes. *Third panel:* Same as in second panel, except that the ellipticity distribution is measured at the time of first infall. *Bottom panel:* Same as in third panel, but with the subhalo sample restricted to those subhaloes that have fallen into the main halo between 0.5 and 3 Gyr.

Finally, when comparing the ellipticities at infall, the difference between dark and luminous subhaloes vanishes when considering systems that were accreted in the same infall time window (bottom panel of Figure 2.6). This is because satellites that fall in early tend to be on slightly more radial orbits, as suggested by Wetzel (2011). Selecting systems with similar infall times removes this dependence and brings the ellipticity distribution of dark and luminous subhaloes into agreement.

We conclude that the orbital difference between dark and luminous subhaloes shown in Figure 2.4 is due to the combined effects of mass-dependent dynamical evolution after infall, a dependence of ellipticity with infall time, and by the selection bias introduced by considering only systems within the virial radius.

Table 2.1: Data for Milky Way satellites taken from the literature. Proper motions are given in equatorial coordinates; distances and velocities have been converted to a Galactocentric frame.

Galaxy	M_V	μ_α (mas/century)	μ_δ (mas/century)	$D_{\rm MW}$ (kpc)	V_r (km/s)	V_t (km/s)	References
Ursa minor	-8.8	-50.0 ± 17.0	22.0 ± 16.0	78 ± 3	-58.5 ± 6.4	157.8 ± 54.8	0,1,2
Carina	-9.1	22.0 ± 9.0	15.0 ± 9.0	107 ± 6	-4.8 ± 3.9	94.9 ± 40.1	3,4,5
Sculptor	-11.1	9.0 ± 13.0	2.0 ± 13.0	86 ± 6	78.0 ± 5.1	243.8 ± 52.9	6,7,5
Fornax	-13.4	47.6 ± 4.6	-36.0 ± 4.1	149 ± 12	-38.8 ± 1.9	185.9 ± 45.3	8,4,5
Leo II	-9.8	10.4 ± 11.3	-3.3 ± 11.5	236 ± 14	14.9 ± 4.3	312.4 ± 118.5	9,10,11
Leo I	-12.0	-11.4 ± 3.0	-12.6 ± 2.9	258 ± 15	167.6 ± 1.6	106.6 ± 34.0	12,13,14
SMC	-16.8	75.4 ± 6.1	-125.2 ± 5.8	61 ± 4	-9.8 ± 2.8	256.3 ± 32.7	15,16,17
LMC	-18.1	195.6 ± 3.6	43.5 ± 3.6	50 ± 2	67.2 ± 4.0	342.5 ± 20.9	15,18,19
Sagittarius dSph	-13.5	-275.0 ± 20.0	-165.0 ± 22.0	18 ± 2	140.9 ± 3.9	274.2 ± 32.7	20,21,22

References: 0=Piatek et al. (2005), 1=Carrera et al. (2002), 2=Walker et al. (2009b), 3=Piatek et al. (2003), 4=Pietrzyński et al. (2009), 5=Walker, Mateo & Olszewski (2009a), 6=Piatek et al. (2006), 7=Pietrzyński et al. (2008), 8=Piatek et al. (2007), 9=Lépine et al. (2011), 10=Bellazzini, Gennari & Ferraro (2005), 11=Walker et al. (2007), 12=Sohn et al. (2013), 13=Bellazzini et al. (2004), 14=Mateo, Olszewski & Walker (2008), 15=Piatek, Pryor & Olszewski (2008), 16=Udalski et al. (1999), 17=Harris & Zaritsky (2006), 18=Clementini et al. (2003), 19=van der Marel et al. (2002), 20=Pryor, Piatek & Olszewski (2010), 21=Monaco et al. (2004), 22=Ibata, Gilmore & Irwin (1994)

2.4 Application to the Milky Way

One main conclusion of the previous analysis is that cosmological simulations make well-defined predictions for the ellipticity distribution of satellite galaxies. These predictions can not be compared directly to observations because the only available data are instantaneous positions and velocities for those satellites with distance, radial velocity, and proper motion estimates. A literature search yields such data for nine of the thirteen Milky Way satellites brighter than $M_V = -8$. These positions and velocities may be used to estimate orbital ellipticities after assuming a mass profile

for the Galaxy. This allows us to place constraints on the total mass of the Galaxy by requiring that the ellipticity distribution matches that of simulated luminous satellites. We pursue this idea in Section 2.4.2, after presenting the observational data set we use in Section 2.4.1.

2.4.1 Milky Way satellite ellipticities

We summarize in Table 2.1 the Milky Way satellite literature data used in our analysis. When several different estimates are available we have adopted values from the recent compilation of McConnachie (2012). We have exclusively adopted proper motion estimates from HST data.

In order to facilitate comparison between observation and simulation we have transformed all values to a Cartesian Galactocentric coordinate system, with the x-axis pointing in the direction from the Sun to the Galactic Centre, y-axis pointing in the direction of the Sun's orbit, and z-axis pointing towards the Galactic North Pole. We assume a velocity of $V_0 = 239 \pm 5$ km s^{-1} for the clockwise circular velocity of the local standard of rest (LSR; McMillan, 2011); $R_0 = 8.29 \pm 0.16$ kpc for the distance from the Sun to the Galactic Centre, as well as $(U, V, W) = (11.10 \pm 1.23, 12.24 \pm 2.05, 7.25 \pm 0.62)$ km s^{-1} for the Sun's peculiar velocity with respect to the LSR from Schönrich, Binney & Dehnen (2010).

We compute ellipticities for all nine satellites assuming that the mass profile of the Galaxy may be approximated by an NFW halo with concentration given by the mass-concentration relation of Neto et al. (2007). We have explicitly verified that the results we quote are insensitive to the exact value of the concentration: for example, varying c between 8 and 17 for a halo of virial mass $M_{200} = 1.1 \times 10^{12}\, M_\odot$ leads to an average change in the ellipticity of 0.05 over all nine satellites. This variation is much smaller than the uncertainty implied by the relatively poor precision of the proper motion estimates.

The coloured lines in Figure 2.7 show how the ellipticities estimated for each MW satellite change as the assumed mass of the Milky Way is varied from $M_{200} = 5 \times 10^{11}$ to $5 \times 10^{12}\, M_\odot$. As anticipated in Section 2.1, the ellipticity of a satellite depends sensitively on the mass of the Galaxy. For example, if a satellite's radial velocity is much smaller than its tangential velocity, then it must be either close to apocentre or pericentre. If near pericentre, increasing the Galaxy mass will decrease its apocentric radius and make the orbital ellipticity decrease. If near apocentre, then the pericentre

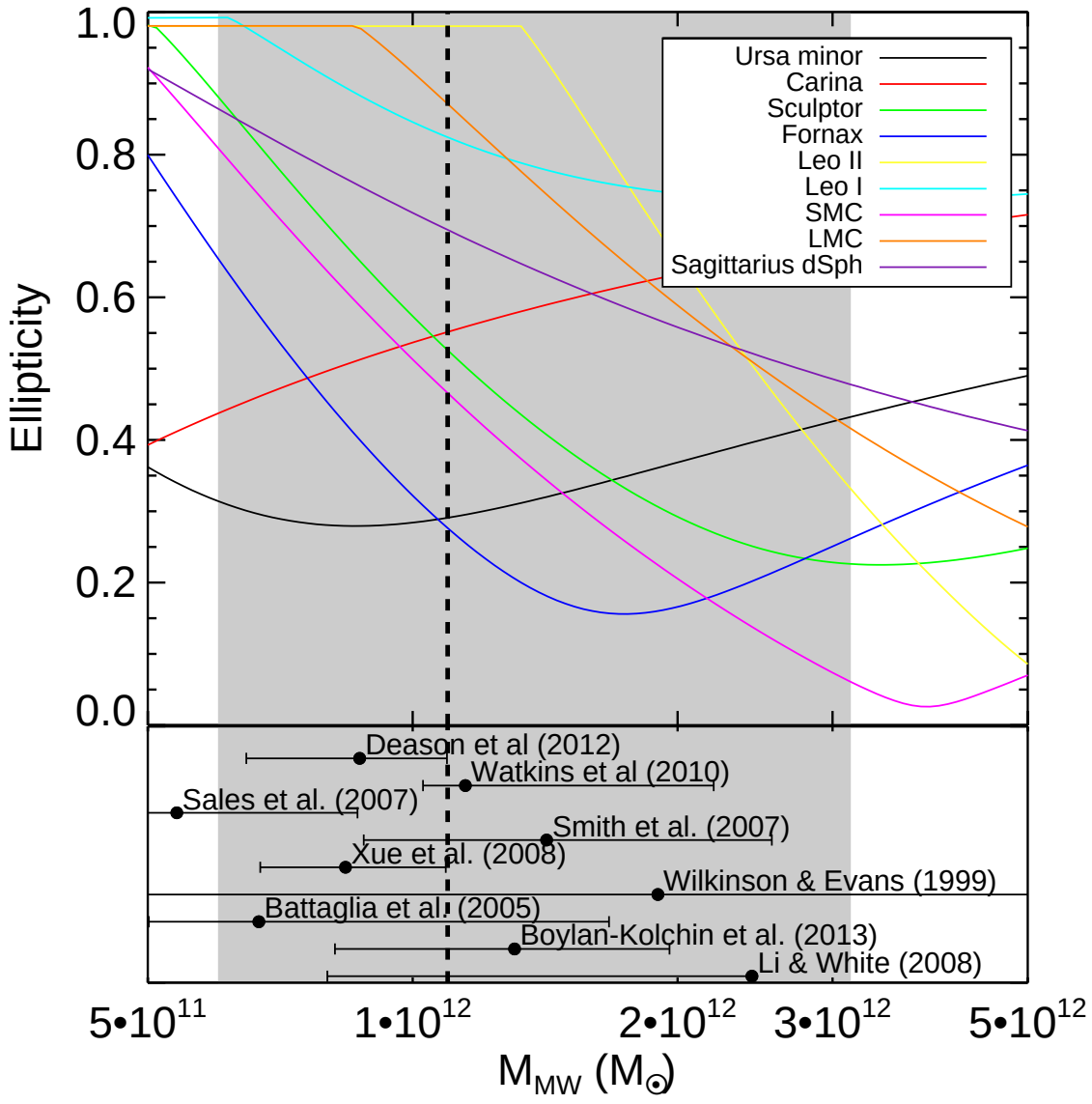

Figure 2.7: The ellipticity of orbits computed for all MW satellites with proper motion measurements (given in Table 2.1) as a function of the assumed MW virial mass. The vertical dashed line gives the most likely MW mass as determined in this work and the grey area the 95% confidence limits. The bottom panel shows MW virial mass estimates from various literature sources, converted to M_{200} (see text for details).

decreases as the mass increases, resulting in a more elliptical orbit instead[3].

We note that a number of previous studies have suggested a possible connection between episodes of star formation history in satellites and pericentric passages during their orbits around the MW (e.g., Mayer et al., 2007; Pasetto et al., 2011; Nichols, Lin & Bland-Hawthorn, 2012). The strong dependence of the timing of such episodes on the assumed mass of the Milky Way provides an interesting constraint. It would be particularly interesting, for example, to see if the *same* Milky Way mass leads to synchronized pericentric passages and star formation episodes for a number of satellites, an issue we plan to address in future work.

2.4.2 The Mass of the Milky Way

As Figure 2.7 makes clear, in general the lower the total mass the larger the inferred orbital ellipticity of a satellite. For example, the median ellipticity of the nine MW satellites increases from 0.4 to 0.98 as the mass is varied in the range described above. The corresponding cumulative ellipticity distribution for several distinct choices of the Milky Way mass is shown in the top panel of Figure 2.8 (coloured lines) and compared with that of classical satellites in Aquarius (thin grey lines for individual haloes and a thick black line for all haloes combined).

Note that the ellipticity distributions of individual Aquarius haloes are very similar despite large differences in their accretion history and the fact that they span a sizable mass range (Springel et al., 2008). Even Aq-F, which underwent a recent major merger and is thus an unlikely host for the Milky Way, is indistinguishable from the rest. We caution, however, that our analysis is based on only six haloes, which precludes a proper statistical study of the halo-to-halo scatter. Future simulations should be able to clarify this, as well as the possible dependence of satellite properties as a function of halo mass and environment. Encouragingly, our conclusion agrees with the earlier work by Gill et al. (2004), who analyse eight simulations chosen to sample a variety of formation histories, ages and triaxialities and report a striking similarity in the ellipticity distribution of their satellite systems. Furthermore, Wetzel (2011) find that the ellipticity distribution of satellites at $z = 0$ is independent of host halo mass in systems less massive than $\sim 4 \times 10^{12} M_{\odot}$, a range that comfortably includes most current estimates of the MW virial mass.

[3]These comments assume that the satellite remains bound as the Galaxy mass changes. Note that Leo I, Leo II, and the Large Magellanic Cloud would be unbound if the Milky Way virial mass was less than 6×10^{11}, 1.5×10^{12}, and $8 \times 10^{11} M_{\odot}$, respectively.

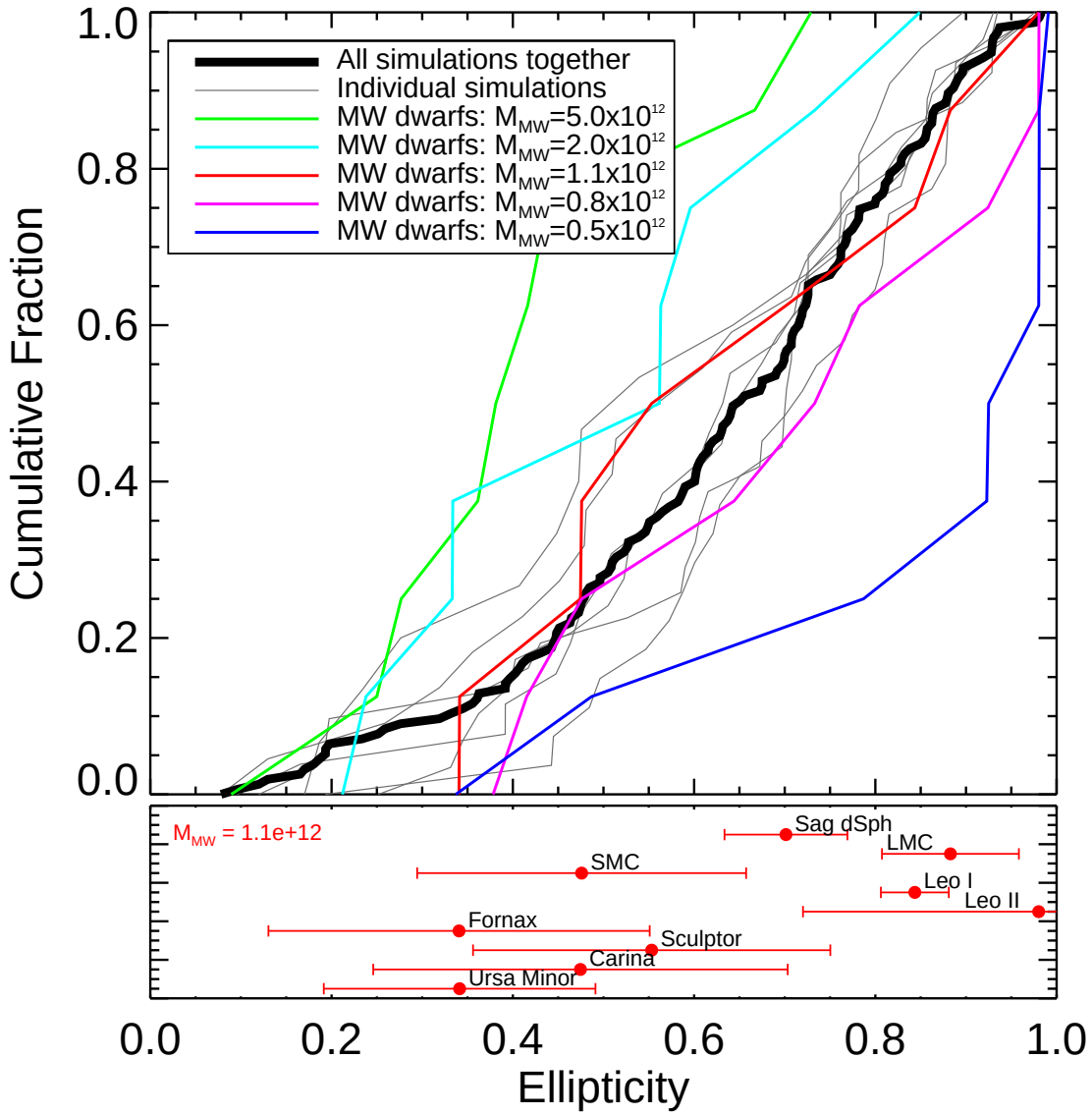

Figure 2.8: *Top panel:* Cumulative ellipticity distributions of classical satellites from Aquarius haloes. Results for individual haloes are shown in thin grey; that for all six haloes combined is shown in thick black. Coloured lines show the ellipticity distribution of the nine classical dwarfs for which data are available, assuming different values for the virial mass of the Milky Way (see legends). *Bottom panel:* Ellipticities estimated for each MW dwarf (arbitrarily offset in y for clarity) assuming the best match halo virial mass for the Milky Way from this work, $M_{200} = 1.1 \times 10^{12} M_{\odot}$. One sigma error bars are given.

We conclude that comparing MW satellite ellipticities with the simulation predictions offers a viable alternative method for estimating the Milky Way mass. The best match (as measured by the maximum value of the KS probability obtained when comparing the nine MW satellite ellipticities to all six Aquarius haloes) is obtained for $M_{200} = 1.1 \times 10^{12} M_{\odot}$. Values less than $6 \times 10^{11}\, M_{\odot}$ or larger than $3.1 \times 10^{12}\, M_{\odot}$ are disfavoured at better than 95% confidence according to the same test.

The bottom panel of Figure 2.8 shows the ellipticities for all satellites for the favoured Milky Way mass including 1σ error bars. Lux, Read & Lake (2010) show that measurements with Gaia's expected accuracy will enable calculations of the last apo- and pericentres of each orbit to an accuracy of $\sim$14% for a given MW potential, whereas current observational data only allow recovery to $\sim 40\%$ accuracy. The Gaia data set will thus greatly enhance the accuracy of the Milky Way mass determination using this method.

In Figure 2.7 the currently favoured mass range is shown by the black dashed line and grey shaded area. We compare in the same figure our results with independent estimates based on a variety of methods, from the timing argument (Li & White, 2008), to the kinematics of halo stars (Battaglia et al., 2005; Smith et al., 2007; Xue et al., 2008; Deason et al., 2012), to virial estimates based on satellite kinematics (Wilkinson & Evans, 1999; Battaglia et al., 2005; Sales et al., 2007a; Watkins, Evans & An, 2010; Boylan-Kolchin et al., 2013). When other mass definitions were used, the estimates given in these papers have been converted to M_{200} assuming NFW profiles with concentrations computed from Neto et al. (2007). Some of these values require extrapolating masses measured within smaller radii out to the virial radius. In spite of this, it is striking that all literature values are in reasonable agreement with our determination, lending support to the viability of our method.

2.4.3 The associated satellites of the Milky Way

As discussed in the previous section, a number of satellites associated with the main halo are found today beyond the formal virial boundaries of the halo. Although this applies mostly to low-mass subhaloes, a small fraction ($\sim 20\%$) of luminous satellites outside r_{200} at $z = 0$ have also been associated with the main halo. Can we use their orbits to identify them? This is important because associated satellites are more likely to have experienced tidal and ram-pressure stripping and to have evolved differently from "field" dwarfs.

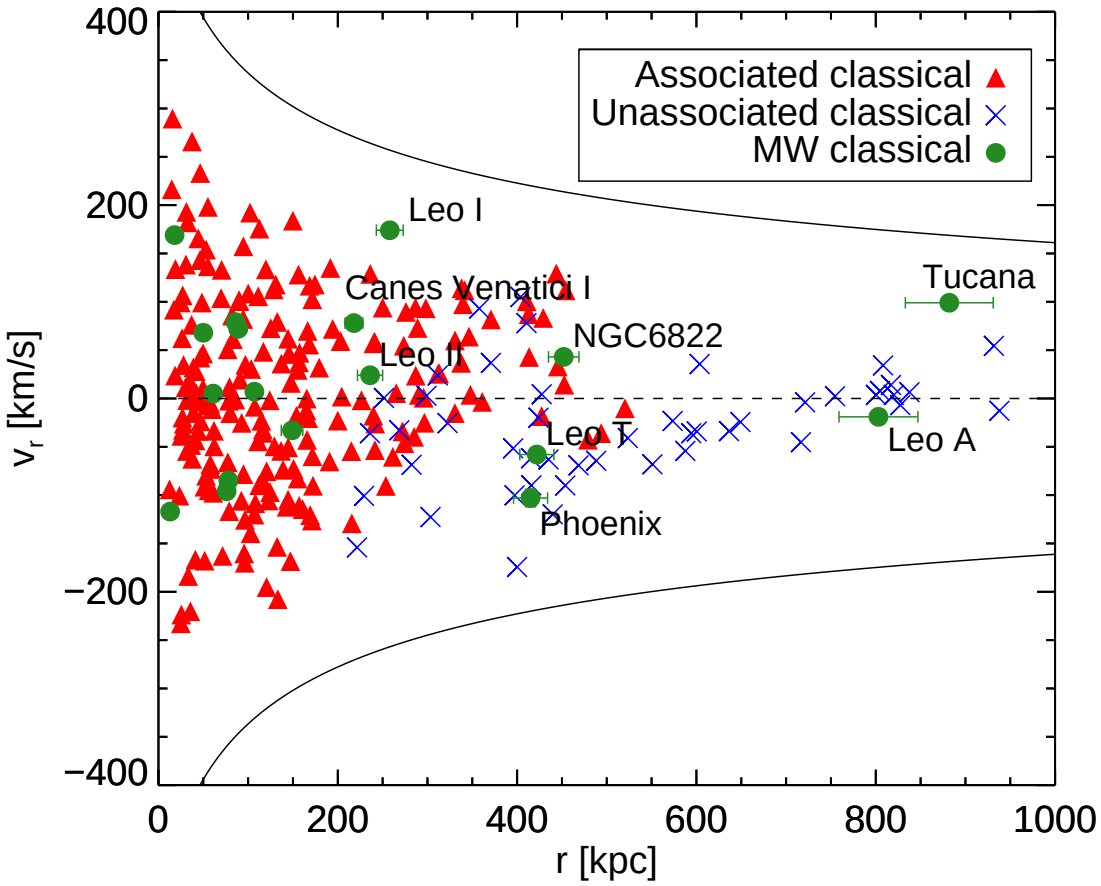

Figure 2.9: Radial distance of classical subhaloes in the Aquarius simulations versus their radial velocity. All Aquarius subhalo data have been scaled to the best-fitting virial mass of $M_{200} = 1.1 \times 10^{12} M_{\odot}$ as derived in the previous section. Red triangles correspond to the associated classical subhaloes (i.e. subhaloes that have at some time been inside the virial radius of the main halo) whereas blue crosses are classical subhaloes that have never been within the main halo. Overplotted in green filled circles are the classical dwarf galaxies within the Local Group that have the MW as their nearest massive neighbour (i.e. galaxies that are closer to M31 than to the MW are not included). The solid lines show the escape velocity of the Milky Way, computed assuming an NFW halo with concentration equal to 8.52.

We explore this idea in Figure 2.9, where we compare the Galactocentric radial velocities and distances of "classical" dwarfs in our model and in the vicinity of the Milky Way. The figure includes only Local Group dwarfs that are closer to the MW than they are to the Andromeda galaxy. All Aquarius main haloes have been normalized to $M_{200} = 1.1 \times 10^{12} M_{\odot}$, our best match Milky Way mass as determined in the previous section. Associated model dwarfs are plotted with red triangles and blue crosses denote dwarfs that have never been associated with the main halo.

Interestingly, most subhaloes located between ~ 300 kpc and ~ 500 kpc that are moving away from the main galaxy are "associated", whereas those with negative radial velocity tend to be unassociated dwarfs on first infall. Furthermore, beyond ~ 600 kpc no classical dwarf has been associated with the main halo.

Some of these conclusions are in apparent conflict with the results obtained by Teyssier, Johnston & Kuhlen (2012), who use associated subhaloes from the Via Lactea II simulation and report a significant population of associated subhaloes out to 1.5 Mpc from the host halo. One important reason for this apparent conflict is that Teyssier, Johnston & Kuhlen (2012) do not discriminate between subhaloes likely to host a dwarf as bright as a "classical" dSph. Indeed, some associated subhaloes in Aquarius are also found beyond 1 Mpc, but these are exclusively low-mass haloes unlikely, according to our semi-analytical model, to host dwarfs brighter than $M_V = -8$.

We end with a word of caution, however. Our Aquarius main haloes do not have a massive companion and the simulations therefore do not attempt to reproduce the large scale distribution of matter of the Local Group, where two massive haloes (those surrounding the MW and M31) are about to collide for the first time. The main halo in the Via Lactea II simulation does have a massive neighbour, which results in a much larger turnaround radius for this system when compared to any of the Aquarius systems. The effect of a Local Group environment on the kinematics of outlying dwarfs has not been properly studied yet, but there are indications that it is likely to play an important role in the accretion history of satellite galaxies and in the evolution of neighbouring dwarfs (see, e.g., Benítez-Llambay et al., 2013).

2.5 Summary and Conclusions

We have combined the semi-analytical modelling of Starkenburg et al. (2013) with the high-resolution simulations of the Aquarius project to investigate the orbits of

the satellites of Milky-Way sized haloes in a ΛCDM universe.

We find that the orbital ellipticity distribution of luminous satellites shows little halo-to-halo scatter and is radially biased relative to that of all subhaloes "associated" with the main halo. The bias is relatively mild, considering that luminous satellites populate preferentially massive subhaloes and are more centrally concentrated than the main subhalo population. The bias results from the combination of three main effects: (i) selecting subhalo samples only within the virial radius; (ii) dynamical evolution after infall; and (iii) a weak dependence of ellipticity with infall time.

The first arises because many low-mass subhaloes (which dominate by number but are generally dark) have apocentric radii larger than the virial radius and are thus found outside r_{200} at any given time. The second likely results from interactions between substructures, which have a more pronounced effect on low-mass subhaloes. Our results therefore urge caution when selecting only subhaloes within the virial radius, since many associated subhaloes (especially low-mass ones) lie at any given time outside the virial radius.

We have compared the ellipticity distribution predicted for luminous satellites with that estimated for nine Milky Way satellites with available 6D phase-space data. Since the latter depends sensitively on the total mass assumed for the Milky Way, this comparison allows us to place interesting constraints on the Milky Way mass. We find that the ellipticity distribution of MW satellites is consistent with the predicted one (at 95% confidence) only if the MW virial mass is in the range 6×10^{11}-$3.1 \times 10^{12}\, M_{\odot}$. This determination is in agreement with current, independent constraints from other observations, and is subject to improvement as the sample of satellites with proper motion estimates increases and the accuracy of such measurements improves.

In the next chapter, we use the same simulations and SAM to probe deep into the very centres of these luminous satellite galaxies in order to establish a link between their internal structure and their dynamical pasts that can be used to better understand the dSph galaxies of our own MW.

Chapter 3

The effect of tides on the shapes and orientations of dwarf spheroidal galaxy haloes

Abstract

We use the high-resolution cosmological N-body simulation suite of the Aquarius project, coupled with a semi-analytic model of galaxy formation (Starkenburg et al., 2013), to study the shapes and orientations of the gravitational potential of "classical" ($M_V < -8$) dwarf spheroidal (dSph) galaxies. The excellent resolution of Aquarius allows us to probe deep into the gravitational potential of these haloes, down to radii comparable to that of the luminous components of dSphs in the Local Group.

As in earlier work, we find that the haloes of classical dSphs are quite triaxial in their centres and become more spherical with radius. Subhaloes, however, tend to be more spherical than field haloes of comparable luminosity due to the influence of the tidal field of their host. We conclude that heavily stripped dSph satellites should be subject to a more spherical gravitational potential than isolated dSphs. We also find a strong preference for satellites to have their major axes aligned with the radial direction to the host halo. This alignment is established after the first close pericentric passage and persists along the orbit, except at subsequent pericentres. Alignment affects primarily subhaloes with a slow initial figure rotation. Our study indicates that "tidal alignment" is a feature that must be taken into account in the calibration of weak-lensing surveys.

3.1 Introduction

Dwarf spheroidal galaxies are important testbeds of current models of galaxy formation and cosmology. Their high mass-to-light ratios of 10 to 1000 (Mateo, 1998; Gilmore et al., 2007; Walker, 2013) indicate that the gravitational potential felt by the stars in these galaxies, and thus their internal dynamics, is dominated by dark, rather than baryonic, matter. Therefore it is appropriate to compare the gravitational potential of satellites in dark matter-only simulations directly with observations of dSphs in our Local Group (modulo possible effects baryons may have on the dark matter distribution in the centres of these galaxies; see the cusp-core debate in Chapter 1). Large samples of line-of-sight (LOS) velocities for individual stars in dSphs have been measured, and allow us to constrain models of the dark matter structure in these galaxies (Kleyna et al., 2002; Walker et al., 2007; Mateo, Olszewski & Walker, 2008; Battaglia, Helmi & Breddels, 2013).

One issue with such models is that the interpretation of radial velocities is highly dependent on model assumptions. Critical might be the often-used assumption of spherical symmetry in the system. Not only do ΛCDM simulations predict dark matter haloes to be generally triaxial (Jing & Suto, 2002; Hayashi, Navarro & Springel, 2007; Vera-Ciro et al., 2011; Allgood et al., 2006; Kuhlen, Diemand & Madau, 2007; Schneider, Frenk & Cole, 2012), but the luminosity profiles of dSphs have been observationally found to be non-spherical (Irwin & Hatzidimitriou, 1995; Martin, de Jong & Rix, 2008). Recently, Hayashi & Chiba (2012) fit axisymmetric dark matter profiles to the LOS velocity dispersions for six dSphs in the MW, finding that the best fit profiles deviate significantly from spherical symmetry – an effect that can significantly alter inferred properties of these galaxies. An understanding of the triaxiality of the gravitational potential in dSph dark matter haloes is thus crucial to our understanding of these faint systems.

With the current suites of high-resolution simulations, it has recently become possible to study theoretically the shapes of dSphs in this (MW-mass) regime. Recent work includes that of Kuhlen, Diemand & Madau (2007) who studied the shapes of all dark matter subhaloes of a MW-sized host galaxy. In this chapter we go a step further and study the shapes of dark matter subhaloes that are most likely to contain dSph galaxies. This specific focus is important since most of the substructure (which is lower-mass and thus remains "dark") may have very different properties than the higher-mass haloes likely to harbour dSphs (Barber et al., 2014).

Vera-Ciro (2013) also combined the Aquarius simulations with the semi-analytic model of Starkenburg et al. (2013) to measure the shapes of dark matter subhaloes that are likely to contain dSph galaxies. However, they focus on the outer (1 to 10 kpc) regions of these subhaloes, beyond the typical half-light radius of $\sim 200 - 500$ pc of MW dSph satellites. Armed with the same simulation suite and semi-analytic model, in this paper we study the shapes of these systems in further detail, particularly in the very inner regions where the stars of dSphs are typically found. In doing so, we relate the measured shapes and orientations of these galaxies to their evolutionary history and environment.

Many studies measure triaxiality by fitting triaxial ellipsoids to the moment of inertia tensor, which is closely related to the density of the system (eg. Kuhlen, Diemand & Madau, 2007; Knebe et al., 2010; Vera-Ciro, 2013). The issue with this approach is that the isodensity contours are often far from being triaxial ellipsoids due to the prevalence of substructure surrounding dark matter haloes (Springel, White & Hernquist, 2004; Hayashi, Navarro & Springel, 2007). The gravitational potential, however, is much less sensitive to local density variations as it depends on the total mass distribution of the halo, and is thus much better fit by ellipsoids. Additionally, the dynamics of the stars in dSph galaxies are dominated not by the local density, but by the gravitational potential of the dark matter halo. Thus, the shape of the potential, rather than the density, should be more relevant to observations of stellar kinematics in dSphs. Hayashi, Navarro & Springel (2007) measure the shape of the gravitational potential in simulated dark matter haloes that have evolved in isolation. As well as investigating the shapes of the gravitational potential in isolated dSphs, in this chapter we go one step further and investigate the effect of an external tidal field on the shapes of satellite galaxy haloes.

The excellent resolution of Aquarius, combined with our careful measurements of shapes, allow us to study other observed properties of these satellite galaxies. It has been found both observationally (Hawley & Peebles, 1975; Djorgovski, 1983; Pereira & Kuhn, 2005; Agustsson & Brainerd, 2006; Faltenbacher et al., 2007) and in simulations (Kuhlen, Diemand & Madau, 2007; Faltenbacher et al., 2008; Knebe et al., 2008, 2010; Pereira, Bryan & Gill, 2008; Pereira & Bryan, 2010; Vera-Ciro, 2013) that satellite haloes of larger systems (eg. galaxy groups and clusters) tend to have their major axes oriented toward the centre of their host. Studying these alignments can tell us about the impact of environment on the formation and evolution of galaxies, and can also be important in the calibration of weak lensing surveys, which often

assume that lensed galaxies are intrinsically oriented randomly in space (Smith et al., 2001; McKay et al., 2001).

Some recent studies have found the radial alignment signal to be less significant in observations of the stellar components of satellite galaxies in galaxy groups and clusters than predicted in dark matter simulations (Bernstein & Norberg, 2002; Adami et al., 2009; Hung & Ebeling, 2012; Schneider et al., 2013). This discrepancy can be resolved only if the physical mechanism for alignment is properly understood. There are in general two mechanisms proposed in the literature. One is a primordial origin, where galaxies are tidally torqued by the surrounding large-scale tidal field during their formation (Peebles, 1969). In that case one would expect the alignment to be strongest in the outskirts of clusters, since galaxy interactions would erase these initial orientations over time. More recently, an alternative mechanism was proposed by Pereira & Kuhn (2005), who claim that tidal interactions between satellites and their host systems may be responsible for a radial alignment that persists over many orbits.

Some studies (eg. Pereira, Bryan & Gill, 2008; Pereira & Bryan, 2010; Knebe et al., 2010) have suggested that tidal torquing by the main halo at pericentric passages may cause this alignment, while others (eg. Kuhlen, Diemand & Madau, 2007) have proposed that the alignment may be due to stretching along the direction of (highly radial) orbits as a result of tidal stripping. Due to the lack of consensus on this topic, we investigate here whether there is a tendency for luminous subhaloes of MW-sized galaxies to align radially, and by tracking them back in time, pinpoint when they become aligned in order to determine the physical mechanism responsible for it.

This chapter is organised as follows. In Section 3.2 we describe the N-body simulations and semi-analytic models used to identify luminous satellites around MW-sized haloes. Our potential-fitting method is described in Section 3.3 and we test for numerical convergence in Section 3.4. In Section 3.5 we show results from our shape measurements, while we discuss orientations of dSphs relative to the main halo in Section 3.6. A discussion and conclusions are presented in Section 3.7 and Section 3.8, respectively.

3.2 N-body Simulations

We use the Aquarius project, a suite of N-body cosmological simulations (Springel et al., 2008), to investigate the shapes of dark matter haloes in a ΛCDM universe. In

addition to the merger trees used in the previous chapter, we now also use the particle data itself in order to measure the gravitational potential of these dark matter haloes. The semi-analytic model of Starkenburg et al. (2013) is again adopted in order to identify dark matter haloes that are likely to host dSph galaxies.

Unless otherwise specified we use the high-resolution level-2 version of the Aquarius runs which have particle mass of order $10^4\,\mathrm{M}_\odot$. Only haloes with at least 700 particles are retained for analysis, which implies a minimum halo mass of $7 \times 10^6\,\mathrm{M}_\odot$. This limit was selected to ensure that r_{max}[1] of all haloes are greater than their convergence radii (see Section 3.4).

The effects of baryons on the dark matter are not included in our simulations. Abadi et al. (2010) found that the inclusion of baryons can significantly transform the shape of dark haloes, generally making them more spherical, especially in their inner regions. Their study, however, deals with MW-type galaxies, which have much lower M/L ratios than typical dSphs. Knebe et al. (2010) report that, although baryons can significantly alter the shape of MW-sized haloes, they do not affect the shape or orientation of the satellite galaxies of such systems. Further, Kazantzidis, Abadi & Navarro (2010) find that the formation of a baryonic disc has limited impact on the triaxiality of the surrounding dark matter halo when the disc contributes less than 50 per cent of its circular velocity, which is the case for most dSph and low surface brightness galaxies. Therefore, we do not expect that the inclusion of baryons would significantly affect our results.

3.3 Potential-fitting method

We describe in this section how we estimate the 3D shape of a halo's isopotential contours. The centre of the halo is first found by locating the minimum of the gravitational potential. The potential is computed at any given point by direct summation over all particles in the halo of their contribution to the potential at that point. We measure the potential along 100 isotropic radial rays extending from the centre of the halo at 20 logarithmically spaced distances along each ray. In the case of subhaloes, these rays extend from 0.05 to $10h^{-1}$kpc; only particles identified by SUBFIND as bound to a subhalo are used to compute its gravitational potential.

We then choose 50 logarithmically spaced potential values for which to measure

[1] r_{max} is the radius at which the circular velocity of a halo reaches its peak, V_{max}.

isopotential contours. For each value of the potential, we interpolate along each ray to obtain 100 isotropically distributed points on the isopotential contour corresponding to that value.

We fit an ellipsoid to these points after recentering so that the centre of the ellipsoid is halfway between their extrema in each spatial dimension. The remainder of our procedure closely follows that of Hayashi, Navarro & Springel (2007). We measure the moment of inertia tensor of this distribution of points in order to determine their principal axes and then rotate the points into the basis of this eigenspace. In order to determine the major, intermediate and minor axis lengths (a, b, and c, respectively) we define for each point a normalized radius r_i such that

$$\frac{x_i^2 + y_i^2 + z_i^2}{r_i^2} = \frac{x_i^2}{a^2} + \frac{y_i^2}{b^2} + \frac{z_i^2}{c^2}. \tag{3.1}$$

For any point that lies on the ellipsoid, this equation equals unity and we have $r_i - \sqrt{x_i^2 + y_i^2 + z_i^2} = 0$. Thus we fit an ellipsoid to this set of points by minimizing the quantity

$$S = \sum_i \left(r_i - \sqrt{x_i^2 + y_i^2 + z_i^2} \right)^2 \tag{3.2}$$

with respect to a, b, and c. To do so we alternatingly find roots of the partial derivative of S with respect to these quantities, iterating until S can no longer be minimized.

A demonstration of this procedure is shown in Figure 3.1 for two subhaloes in Aq-A-4: subhalo 1 is very elliptical, while subhalo 2 is quite spherical. The top left panel shows a projected density plot of the main halo, along with the positions of these two subhaloes. The top right panel shows the potential measured along 100 radial rays as a function of radius for these subhaloes, scaled by an arbitrary value for clarity. Here it is already obvious that, at given distance from the centre, subhalo 1 has a wider range of potential values and is thus more elliptical. In the bottom panels, for each subhalo we compare our ellipsoidal fits with the gravitational potential along a 2D plane. For clarity the subhaloes have been reoriented such that x and y lie along their minor and major axes, respectively. A simple by-eye comparison shows that ellipsoids tend to be excellent approximations to the isopotential contours in our dark matter haloes (see also Springel, White & Hernquist, 2004; Hayashi, Navarro & Springel, 2007).

We have attempted to use alternate methods to measure isopotential contours. One such method is that described by Springel, White & Hernquist (2004), where one

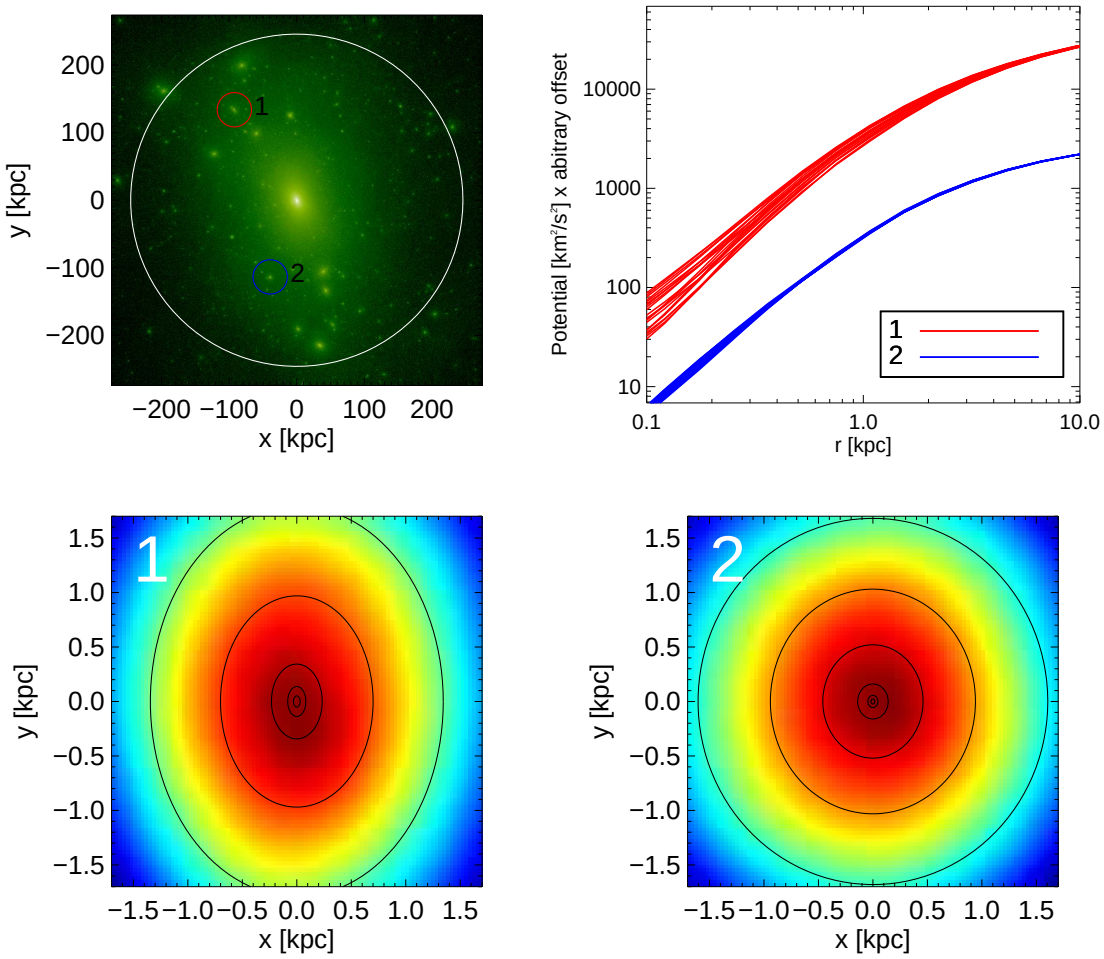

Figure 3.1: Demonstration of our procedure used to fit isopotential contours to dark matter haloes. *Top left panel:* Projected density plot of Aq-A-4. The red and blue circles indicate the positions of our two example subhaloes. *Top right panel:* Gravitational potential as a function of radius along 100 radial rays extending from the respective centres of each subhalo selected in the top left panel. *Bottom panels:* Ellipsoidal fits (black ellipses) to isopotential contours for these subhaloes superimposed on a 2D slice of their gravitational potentials, oriented such that the x and y axes point in the direction of their minor and major axes, respectively. The depth of the potential increases from blue to red.

measures the potential along three uniform grids in orthogonal planes that intersect at the centre of the halo. We tested that our method is less computationally expensive and gives more accurate results near the centre of the halo, where we focus our analysis.

3.4 Numerical Convergence

Because we wish to investigate the shape of the potential in the central parts of a halo at the level of the galaxy, we must understand how the accuracy of our measured shapes changes with radius. We can do this by measuring the axis ratios as a function of radius of a halo at various levels of resolution. Ideally, we would like to perform this test on the subhaloes of the Aquarius main haloes, but to do this we would have to match subhaloes between simulations, a feat which can be done (Springel et al., 2005; Vera-Ciro, 2013) but is non-trivial. For expediency, we take a different approach and test the convergence of our algorithm on the Aq-A main halo at different resolution levels, and apply our findings to all haloes in the simulation.

Specifically, we explore whether the definition of "convergence radius", $r_{\rm conv}$, first proposed by Power et al. (2003) holds for isopotential shapes. These authors show that deviations from convergence in the mass profile occur where the local collisional relaxation time, $t_{\rm relax}(r)$, becomes shorter than the dynamical time at the virial radius, $t_{\rm circ}(r_{200})$, which is of the order of the age of the Universe. The ratio between these two timescales can be written as

$$\kappa(r) \equiv \frac{t_{\rm relax}(r)}{t_{\rm circ}(r_{200})} = \frac{N}{8\ln N}\frac{r/V_{\rm c}}{r_{200}/V_{200}} = \frac{\sqrt{200}}{8}\frac{N(r)}{\ln N(r)}\left(\frac{\overline{\rho}(r)}{\rho_{\rm crit}}\right)^{-1/2}, \qquad (3.3)$$

where $N(r)$ is the number of particles within radius r, $\rho_{\rm crit}$ is the critical density of the Universe, and $\overline{\rho}(r)$ is the mean density within r. The value of κ is chosen so that the circular velocity profile of a halo deviates by less than some desired percentage between different resolutions. For example, $\kappa = 7$ (1) guarantees a maximum error of 2.5 (10) per cent in the circular velocity profile at $r_{\rm conv}$ (Navarro et al., 2010).

We measured the shapes of isopotential contours in the Aq-A main halo at resolutions 1 (highest) through 5 (lowest). The ratios b/a and c/a are shown as a function of radius $r' = (abc)^{1/3}$ in Figure 3.2. The thick lines show the axis ratios down to $r_{\rm conv}(\kappa = 0.1)$, and thin lines inside that radius. The convergence relative to the highest resolution run is excellent down to very small radii, deviating by less than 5 per cent for radii larger than that corresponding to $\kappa = 0.1$. We therefore choose $r_{\rm conv}(\kappa = 0.1)$, hereafter denoted $r_{\rm conv}^{(0.1)}$, as our fiducial convergence radius.

For reference, we also show in Figure 3.2 the axis ratios of *isodensity* contours of the Aq-A-2 main halo measured by Vera-Ciro et al. (2011). Our isopotential contours are much more spherical at all resolutions and radii. This is expected,

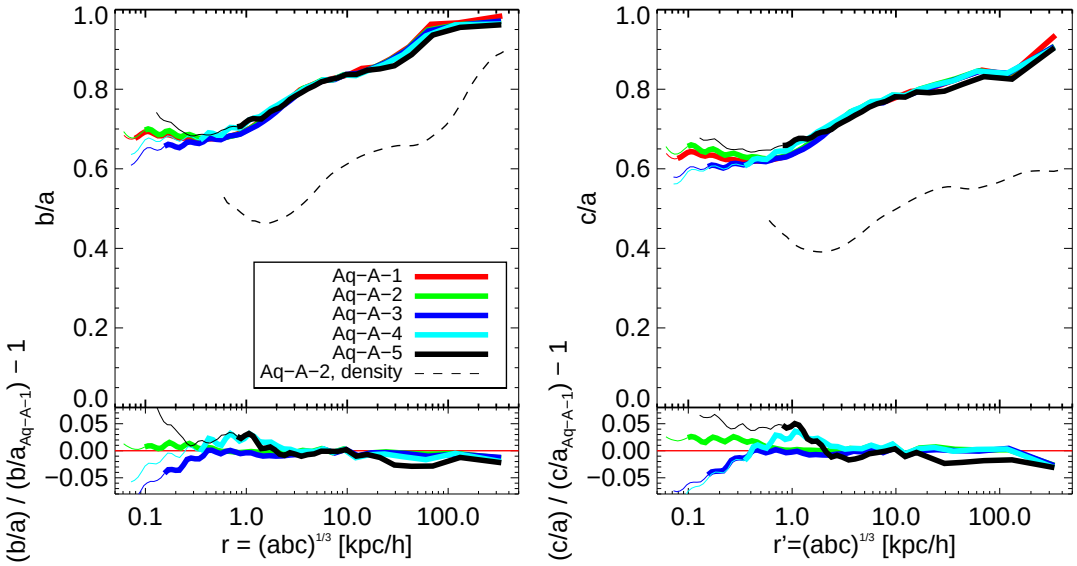

Figure 3.2: Convergence of the measured axis ratios for the Aq-A main halo at five different resolutions. The ratios between intermediate and major axes (b/a) and the minor and major axes (c/a) are shown in the left and right panels, respectively, as a function of radius $r' = (abc)^{1/3}$ from the centre of the halo. Residuals relative to the highest resolution run are shown in the bottom panels. Lines are drawn thinner below our computed convergence radius. Dashed lines indicate the respective axis ratios for isodensity contours in Aq-A-2 from Vera-Ciro et al. (2011).

since isopotential contours are generally more spherical than the mass, and should become more spherical with increasing radius due to the increasing importance of the monopole term.

3.5 Shapes of dwarf galaxies

We now describe the shapes of isopotential contours of subhaloes in the Aquarius simulations. Unless otherwise specified, all results combine the Aq-A through E simulations. Aq-F is excluded due to a recent major merger which is not thought to be representative of the formation of the MW.

3.5.1 Shape as a function of $V_{\rm max}$

As a first test of our method, we perform a similar analysis as Vera-Ciro (2013), who compare the measured axis ratios against $V_{\rm max}$ for all subhaloes and field haloes in the Aquarius simulations. Indeed, we seek to go one step further and see how this

relation applies purely to subhaloes expected to host dSph galaxies.

To reduce computational cost, rather than analysing all haloes in the simulation, we take sample haloes as a function of $V_{\rm max}$ in the range 1 to 35 km s^{-1}. The axis ratios b/a and c/a were computed at $r_{\rm max}$ (as in Vera-Ciro, 2013) and are plotted as a function of $V_{\rm max}$ in the top panels of Figure 3.3. The left and right panels show "field haloes" and "subhaloes", defined as those outside $2r_{200}$ and those within r_{200}, respectively. For easy comparison, log-linear fits to the axis ratios of the field haloes are reproduced in each panel. For field haloes, we see a general trend of decreasing axis ratios with $V_{\rm max}$ that is much stronger in c/a than b/a. Subhaloes, on the other hand, tend to have similar b/a but larger c/a than field haloes at all $V_{\rm max}$. These trends agree qualitatively with the results of Vera-Ciro (2013).

Because we are interested in haloes that host luminous galaxies, we repeat this exercise only for those haloes that are likely to have $M_V < -8$ as determined semi-analytically (Starkenburg et al., 2013). Since dSph galaxies brighter than this limit are typically referred to as "classical" dSphs, we will hereafter refer to dark matter haloes likely to contain such dSphs as "classical haloes". These results are shown in the bottom row of Figure 3.3. Classical field haloes span only a small range in the $V_{\rm max}$ distribution. Since all field haloes with such high $V_{\rm max}$ tend to be classical, it is not surprising that the classical field haloes agree with the high $V_{\rm max}$ end of all field haloes.

Some classical subhaloes, however, have much smaller values of $V_{\rm max}$, due to tidal stripping from the main halo's gravitational potential. Again, the agreement between the population of all subhaloes and classical subhaloes at high $V_{\rm max}$ (> 30 km/s) is not surprising since in this regime nearly all subhaloes are classical. However, at lower $V_{\rm max}$ ($< 20 - 30$ km/s) the classical subhaloes are extremely spherical, even more-so than the general population of dark subhaloes. If these lower-mass classical subhaloes really are tidally stripped, this trend implies that tidal forces cause subhaloes to become rounder, at least at $r_{\rm max}$. In the next subsection we investigate if this trend is present at all radii, and in particular down to radii as small as where stars are expected to be.

3.5.2 Shape as a function of radius

In the previous section we saw that low mass classical subhaloes of MW-sized haloes tend to be much more spherical than high-mass subhaloes, when measured at $r_{\rm max}$.

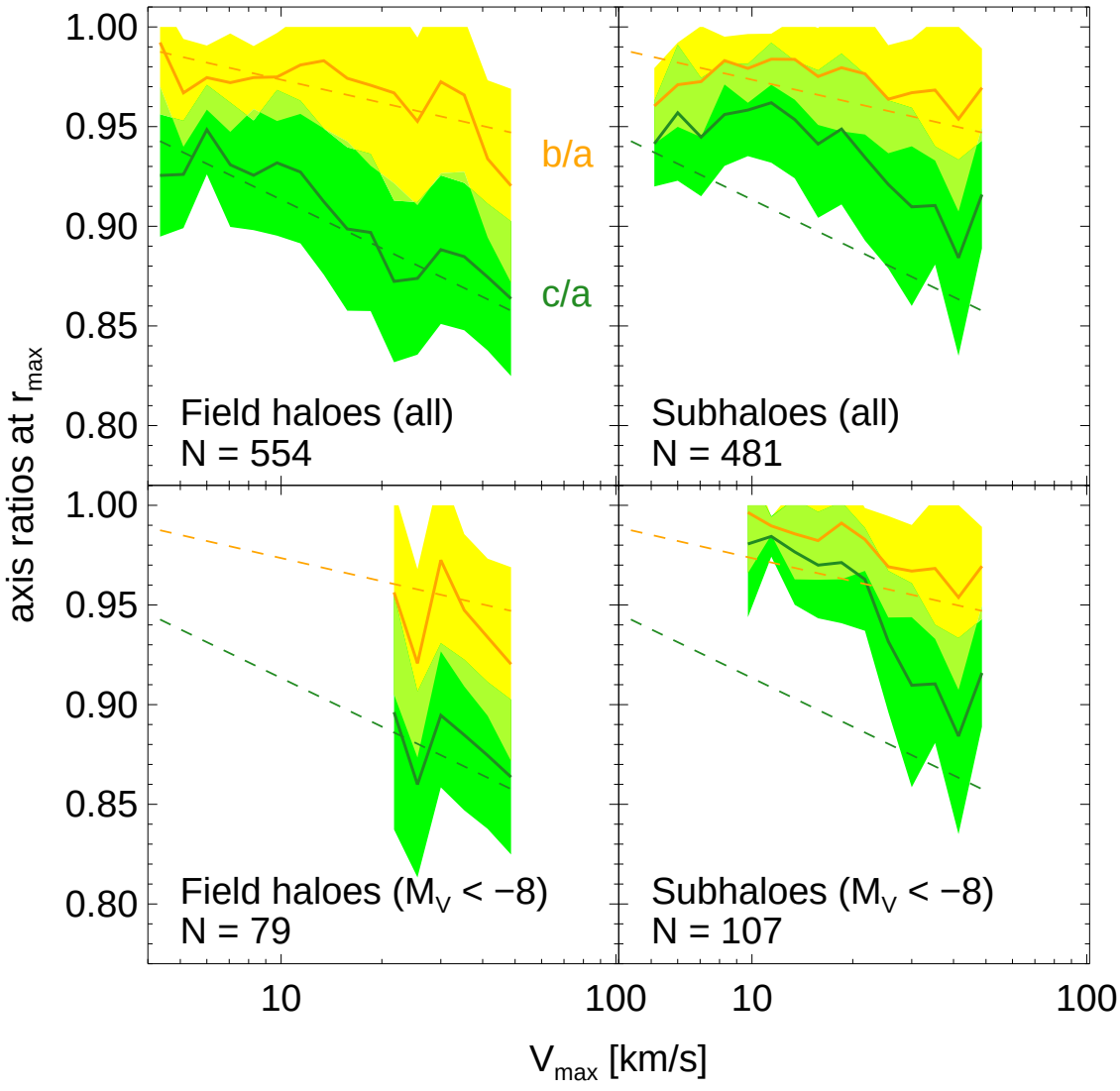

Figure 3.3: Axis ratios as a function of maximum circular velocity of various subsamples of haloes. The left and right columns show haloes in the field ($r > 2r_{200}$) and subhaloes of the main halo ($r < r_{200}$), respectively. The top and bottom rows show haloes of any luminosity and classical haloes, respectively. b/a and c/a are shown in yellow and green respectively. Solid lines indicate running medians while solid filled areas indicate the 1σ scatter. Overlapping regions are coloured in yellow-green. Linear fits (in log space) to the axis ratios shown in the top left panel are reproduced in each panel for reference.

Here we investigate if this trend is measurable in the inner (stellar) regions of these subhaloes.

In Figure 3.4 we show the median axis ratios as a function of the radius at which they are measured for all subhaloes with luminosities comparable to that of the Fornax dSph galaxy (within $\Delta M_V = 0.5$). We sample radii from the convergence radius of ~ 160 pc at this resolution out to nearly 14 kpc. Given that the half-light radius of Fornax is 710 pc (McConnachie, 2012), we are able to measure the axis ratios of the potential deep within the galaxy itself. Medians for those inside and outside r_{200} are shown in red and blue, respectively. For both populations, haloes are very spherical in their outskirts and become more triaxial toward the centre. However, at all radii, those within r_{200} are more spherical on average than those outside r_{200}.

Hayashi, Navarro & Springel (2007) measured the shapes of isopotential contours of simulated dSphs that evolved in isolation. In Figure 3.4 we over-plot their results, which agree extremely well with our haloes outside r_{200}. The Hayashi, Navarro & Springel (2007) results shown here have been scaled from their original plot using $r_s = r_{\rm max,Fornax}/2.16$, where $r_{\rm max,Fornax}$ is the median $r_{\rm max}$ value from our Fornax-like sample. This agreement shows that, in terms of their axis ratios, haloes that are outside of r_{200} today tend to be indistinguishable from those that evolved in isolation.

3.5.3 Luminous subhalo shape convergence

We wish to investigate the shapes of not only Fornax-like classical dSphs, but of lower-mass dSphs as well, such as Ursa Minor and Draco, down to their half-light radii. To do so we must be cautious, since the half-light radii of such galaxies are comparable to the convergence radii of our simulated haloes. In Figure 3.5 we compare the half-light radii of nine MW dwarfs to $r_{\rm max}$ and $r_{\rm conv}^{(0.1)}$ of the (simulated) classical haloes in Aquarius, as a function of M_V. It is worth noting here that $r_{\rm conv}^{(0.1)}$ depends very weakly on M_V, and in fact is roughly constant here. This is expected since $r_{\rm conv}^{(0.1)}$ depends most critically on the number of enclosed particles, which, within a small radius ($\sim 500h^{-1}$pc), varies only weakly with halo mass (Power et al., 2003; Kuzio de Naray & McGaugh, 2014).

The half-light radii of all nine of our MW dSphs are greater than (or equal to, in the cases of Leo II and Ursa Minor) our typical convergence radius of ~ 160 pc. Thus, we should be able to measure the shapes of classical dwarfs in the simulation down to these half-light radii to within an accuracy of around 5%. Also note that

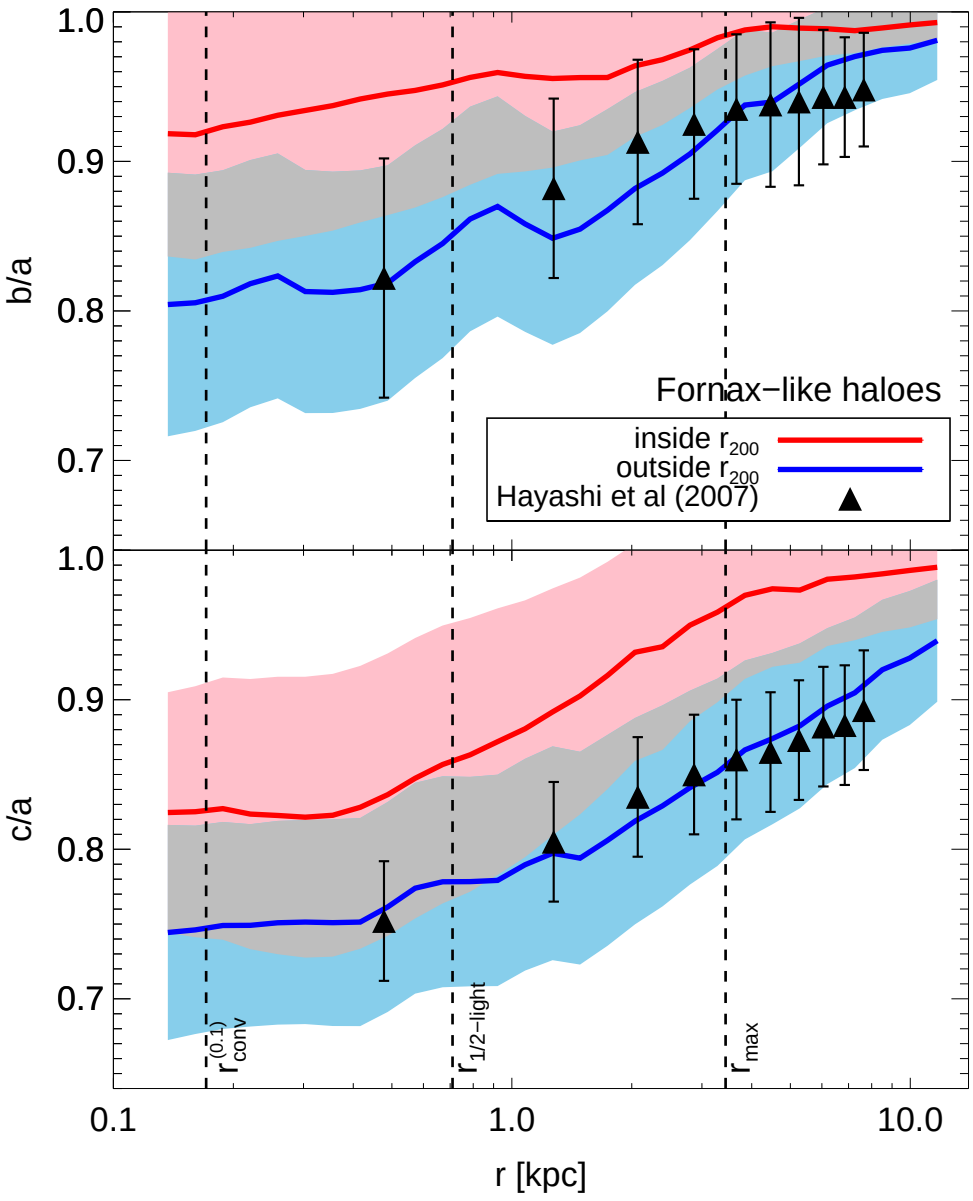

Figure 3.4: Axis ratios as a function of radius for satellites expected to have the same magnitude as Fornax, to within 0.5 magnitudes. Running medians for subhaloes inside and outside r_{200} are shown as red and blue solid lines respectively, while solid filled areas indicate the 1σ scatter. Overlapping regions are plotted in grey. For reference, the same relation for isolated haloes from Hayashi, Navarro & Springel (2007) is shown in black points. The mean convergence radius and mean $r_{\rm max}$ of our Fornax-like haloes, as well as the half-light radius of Fornax itself, are indicated with vertical dashed lines.

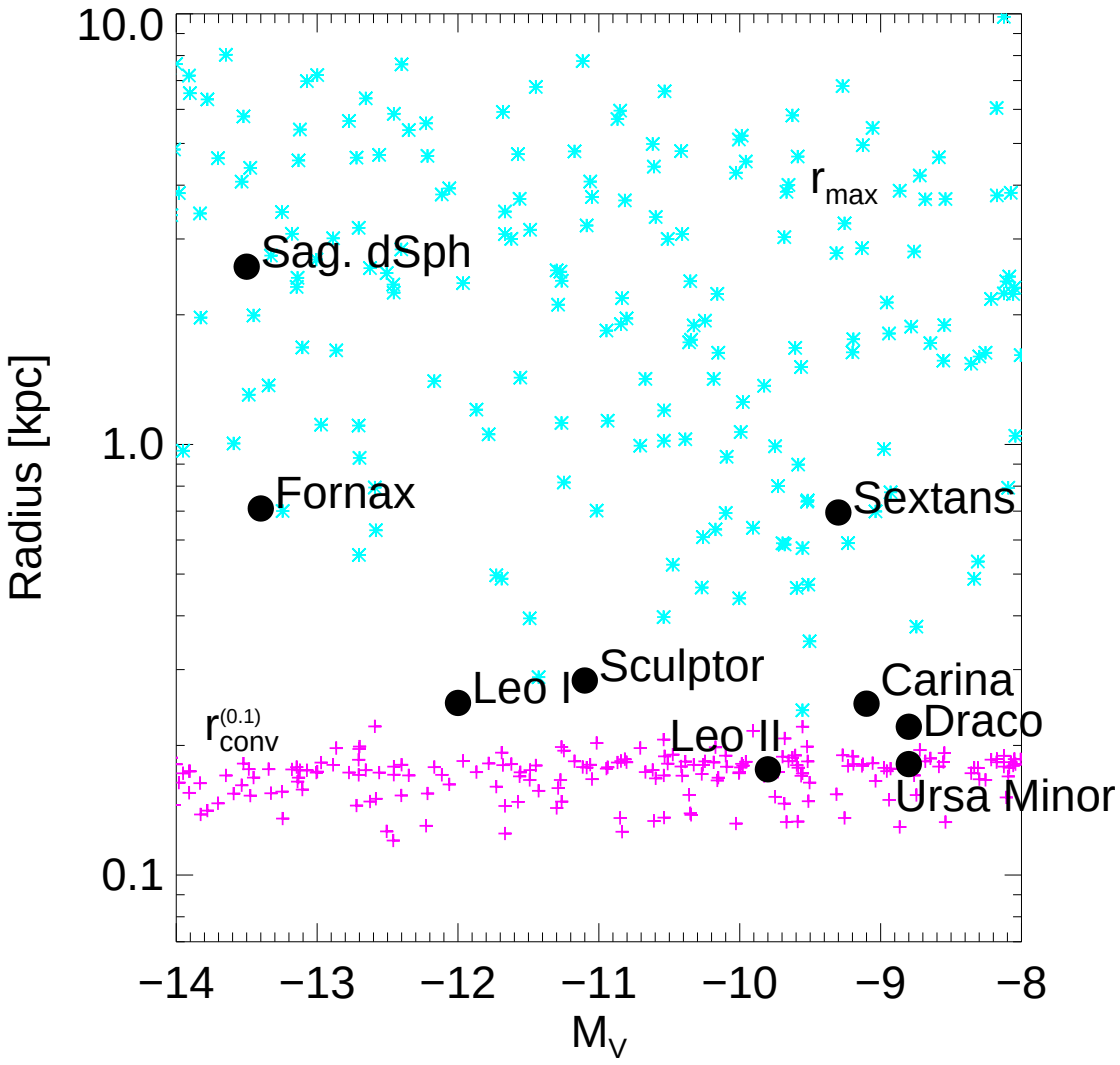

Figure 3.5: Comparison of various scale radii as a function of absolute V-band magnitude. Half-light radii of classical satellites of the MW are shown as large black filled circles. $r_{\rm max}$ and $r_{\rm conv}^{(0.1)}$ of Aquarius classical satellites are shown as cyan stars and magenta crosses respectively.

$r_{\rm max}$ is always above $r_{\rm conv}^{(0.1)}$, indicating that the results for low-mass classical satellites in Figure 3.3 are not affected by resolution effects.

In the next section we will look at all of the classical haloes at once, and use 800 pc as a typical half-light radius. We have checked that using a smaller radius does not affect our results substantially. This may be seen in Figure 3.4, where the axis ratios do not change appreciably below this radius.

3.5.4 Shape as a function of stripping

The results of the previous subsections suggest that haloes that are more stripped are more spherical. To investigate this possible correlation we adopt as a proxy for stripping the ratio between $V_{\rm max}$ at $z = 0$ and the maximum value of $V_{\rm max}$ that the halo ever had (hereafter $V_{\rm max}/V_{\rm max,max}$). In the bottom panel of Figure 3.6 we show histograms of classical haloes inside and outside r_{200} in red and blue respectively. The former population is clearly much more stripped than the latter. Thus if stripping is the cause of this sphericalization, this would explain the more spherical shapes of subhaloes located within r_{200} of the main halo, as seen in Figure 3.4.

In the top two panels of Figure 3.6, we show the axis ratios measured at 800 pc as a function of stripping for those classical haloes inside and outside r_{200} in red and blue, respectively. Black lines indicate running medians of the two populations combined. We also show the corresponding remaining mass fraction on the top axis. We find that subhaloes that have been significantly stripped ($V_{\rm max}/V_{\rm max,max} < 0.7$), are on average much more spherical than those that have not ($V_{\rm max}/V_{\rm max,max} > 0.9$), especially in c/a. Indeed, even the axis ratios of those subhaloes that are within r_{200} but have not yet been stripped appear to match the triaxiality the field halo population. As well, some field haloes that have been stripped (possibly by haloes other than the main halo) tend to be much rounder than those that are non-stripped. Thus, although a subhalo's proximity to the main halo and degree of stripping are correlated, it appears that stripping itself is the main cause of sphericalization of dark matter haloes that are likely to contain dSph galaxies.

3.5.5 Predictions for real MW satellites

We now investigate the axis ratios measured at the half-light radii of subhaloes that are of comparable luminosity to specific MW dSph galaxies (within 0.5 in M_V). As the semi-analytic model does not predict half-light radii for the Aquarius haloes, we measure the shapes at the half-light radii the MW dSph for which the subhaloes are analogues.

In Figure 3.7 we show the b/a and c/a axis ratios as a function of stripping for classical subhaloes that are similar in luminosity to nine MW classical dSph galaxies, as indicated in each panel. Remarkably, this trend of sphericalization with stripping is observable over a wide range in satellite magnitudes, from Draco with $M_V = -8.8$ to the Sagittarius dSph with $M_V = -13.5$. Therefore it is possible to predict whether

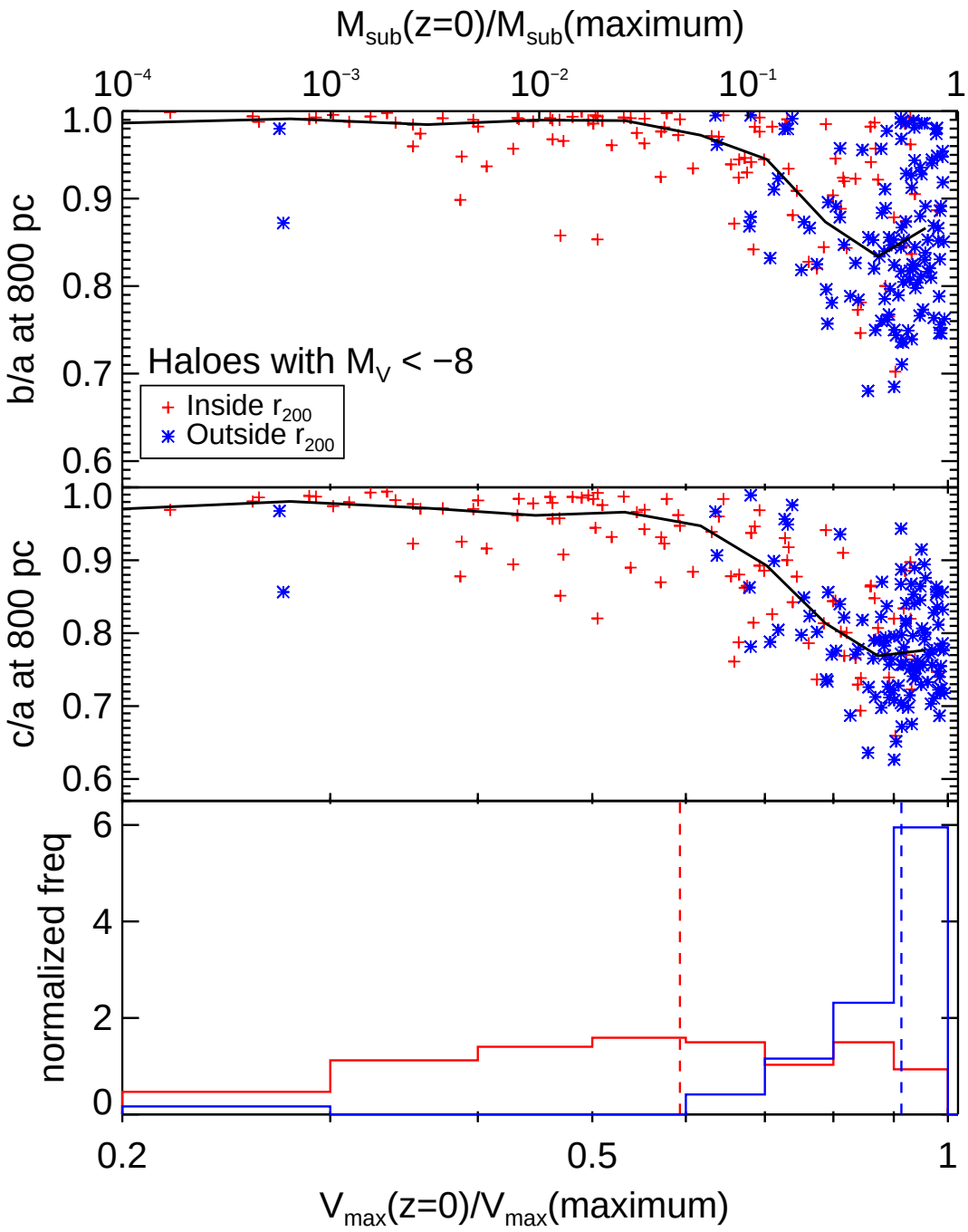

Figure 3.6: Axis ratios measured at 800 pc for all 228 classical haloes in our sample, as a function of stripping represented by the measured $V_{\rm max}$ at $z = 0$ relative to the maximum value that it ever had. Haloes within and outside r_{200} are shown in red and blue, respectively. Black lines indicate running medians.

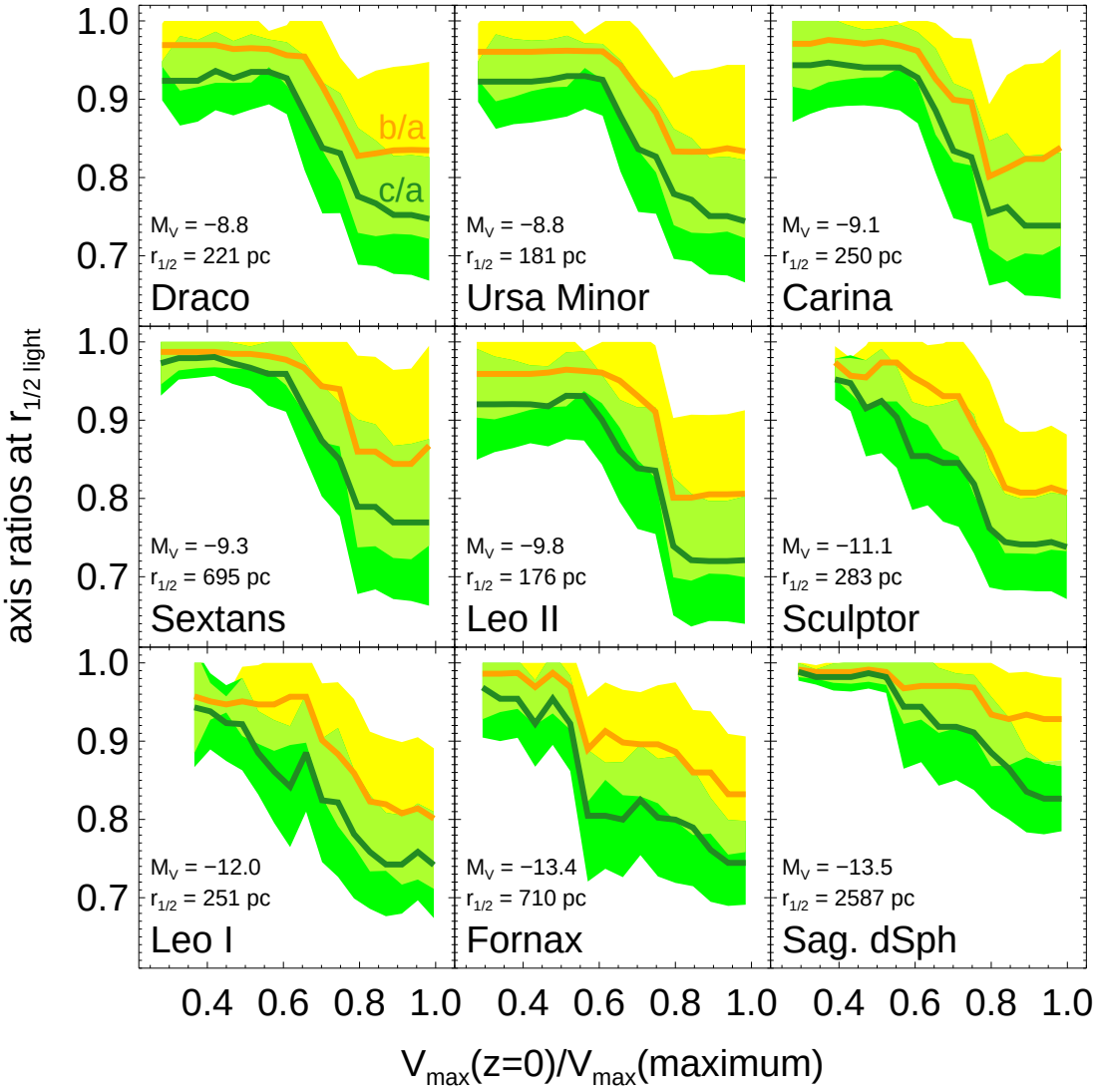

Figure 3.7: As in Figure 3.6, except now including in each panel those subhaloes within 0.5 magnitudes of the indicated MW dwarf in $M_{\rm V}$. Axis ratios are measured at the half-light radius of each MW dwarf. b/a and c/a are shown in orange and green respectively. Dark lines indicate running medians while solid filled areas indicate the 1σ scatter about the medians.

a MW dSph satellite galaxy has been significantly stripped or not given knowledge of the shape of its gravitational potential. For example, if c/a of Fornax is found to be more spherical than 0.9, it is likely that more than 90 per cent of its maximum mass has been stripped away. This result is a robust prediction of ΛCDM and will be a useful tool in understanding the complex dynamical histories of MW dSph galaxies.

3.6 Orientation of dwarf galaxies

We now investigate the orientation of satellite galaxies relative to the direction to the centre of their host halo. In particular we investigate if this alignment is present in the inner regions of classical subhaloes in our simulations and identify clues to a possible physical cause of the alignment.

3.6.1 Methods

For this purpose we study only subhaloes of the main Aquarius haloes, as those in the field should be randomly oriented with respect to the main halo (which indeed we have confirmed). As well, we adopt a threshold of $b/a < 0.95$ for the ellipsoidal fit whose orientation is being measured to ensure that the direction of the major axis is measured accurately. The b/a distribution of the resulting subsample is shown as the grey-filled area in Figure 3.8. Roughly half of the subhaloes have b/a below this threshold, leaving us with 43 classical satellites with $r < r_{200}$ and $b/a < 0.95$.

We have tested the accuracy of our axis direction measurements as a function of our b/a threshold. To do so we create mock NFW haloes that have been artificially flattened to make them triaxial, and orient them such that the major axis should point in the (arbitrary) $\hat{z}$-direction. The orientation of the major axis was then measured while varying b/a. We found that indeed the direction of the major axis begins to deviate significantly from $\hat{z}$ only for haloes that are more spherical than $b/a = 0.95$. Specifically, above this limit the cosine of the angle between them begins to deviate from unity by more than 0.1. Thus, given this cutoff, we expect that our direction measurements are quite accurate. We have checked as well that the value of c/b does not affect our measurement of the direction of a.

3.6.2 Radial alignment with the main halo

We have measured the angle θ between the major axis and the direction to the main halo for all 43 classical subhaloes in our sample. For a population with random orientations, the distribution of $|\cos(\theta)|$ is expected to be uniform.

In Figure 3.9 we plot, from top to bottom, histograms of $|\cos(\theta)|$ measured at 400, 800, and 1600 pc from the centre of each subhalo in our sample, respectively. The alignment is heavily biased toward unity in each panel, indicating a net preference for subhaloes to be aligned with the direction to the centre of the main halo. A

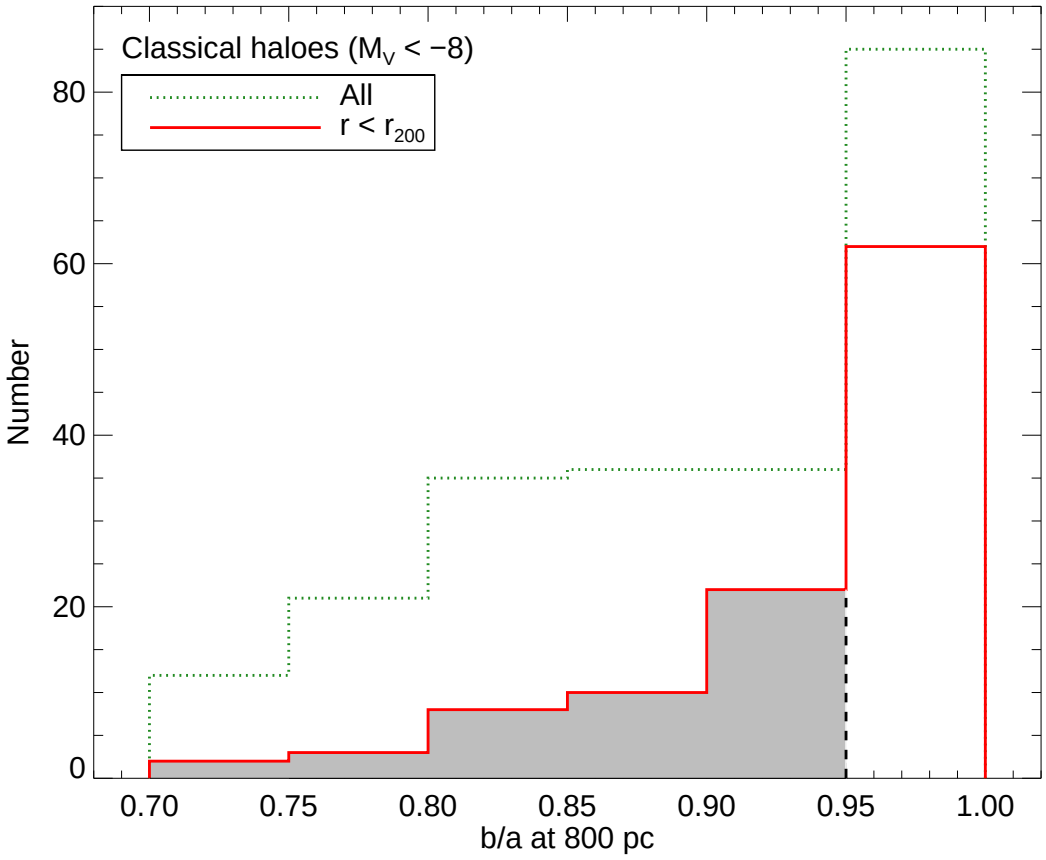

Figure 3.8: Distribution of b/a axis ratios for all classical haloes (green dotted line) and classical subhaloes (red solid line), measured at 800 pc. Classical satellites with $b/a < 0.95$ are shown in grey; this sample is used for orientation measurements in Section 3.6.

KS test indicates that the distribution is significantly different from uniform at the 99% confidence level. The fact that this bias is seen in all panels indicates that the orientation of a halo is independent of measurement radius. Further, we have checked that the major axis direction does not change within a halo as long as b/a remains less than 0.95. This is important, for it implies that the stars in MW dSph satellites must also be subject to a gravitational field that is aligned with the host halo. For reference, we also plot the alignment of classical haloes beyond r_{200}. We find no significant alignment for these haloes, indicating that the alignment in the subhaloes is the result of interactions with the main halo.

We have checked that the measured alignment is not due to numerical effects. One possible source of bias is that in the calculation of the potential we are only using

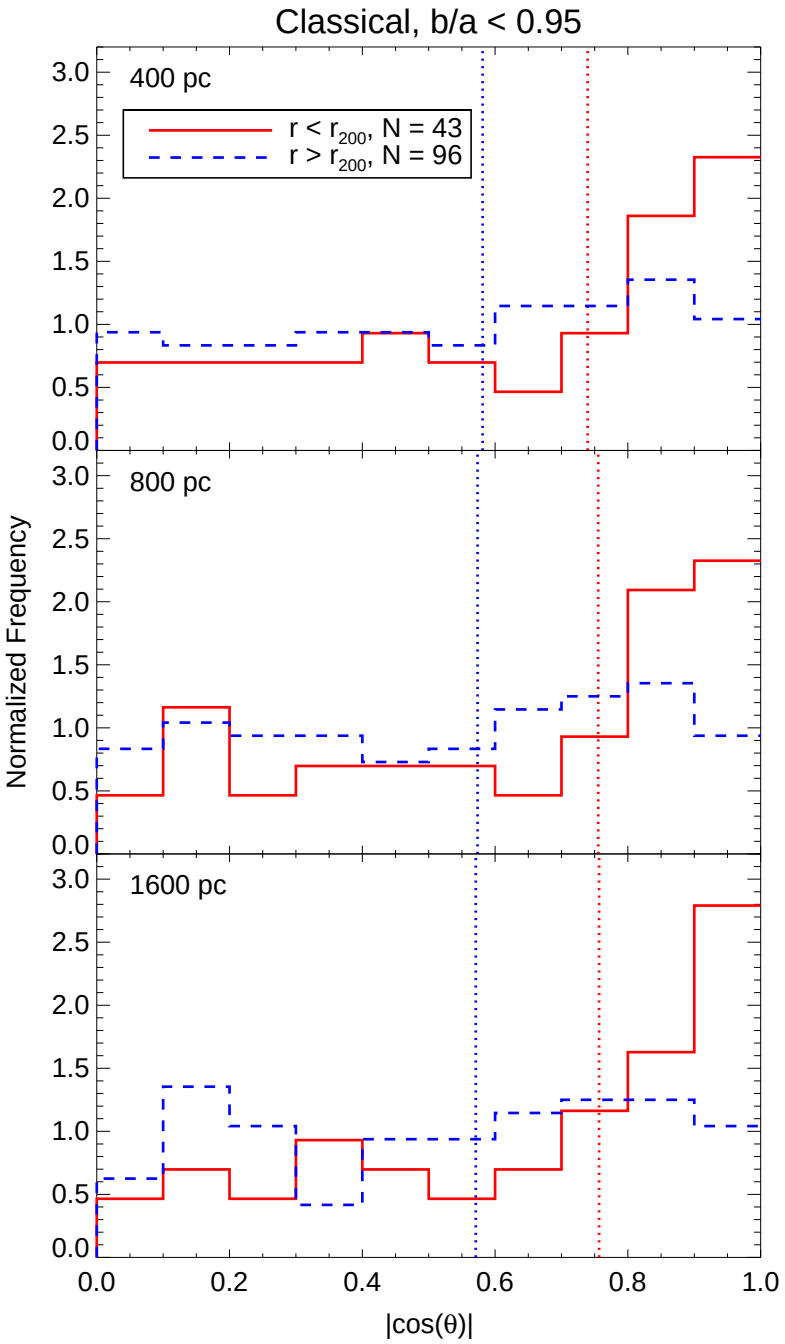

Figure 3.9: Radial alignment of classical ($M_V < -8$) haloes. Subhaloes (with $r < r_{200}$) and field haloes ($r > r_{200}$) are shown in red solid and blue dashed lines, respectively. Vertical dotted lines indicate the median alignment of each population. Alignment is measured at 300, 600, and 1200 h^{-1} pc from the centre of each halo, shown from the top to bottom panels, respectively.

particles identified by SUBFIND. Therefore it is feasible that we may incur a bias in the radial direction of subhalo particles due to the radial density gradient of the main halo, which could cause a bias toward measured radial alignment. To test the importance of this effect, we remeasured the potential of subhaloes that are aligned with the main halo using instead of the SUBFIND selection only particles within 0.5, 1, and 2 $r_{\rm max}$ from the centre of the subhalo. In each case the measured orientations of the subhaloes were not affected.

3.6.3 Alignment examples

In order to understand the origin of the alignment seen in Figure 3.9, we tracked these 43 subhaloes back in time, at each time step measuring the alignment of the major axis with the (instantaneous) centre of the main halo. In this way we can pinpoint when and where a subhalo becomes aligned.

An example of a subhalo aligned with the main halo at $z = 0$ is shown in Figure 3.10. The left panel shows $|\cos(\theta)|$, distance from the main halo, axis ratios measured at 800 pc, and degree of stripping of this subhalo as a function of time since the Big Bang. Important points in the satellite's orbit are shown as vertical lines. Apocentric and pericentric passages are defined as An and Pn respectively, where $n = 1, 2, 3$ correspond to the first, second, third passages respectively. In the right panel we plot the orbit of the satellite projected onto its orbital plane at $z = 0$. Pericentric and apocentric passages are marked with coloured dots. This subhalo initially falls into the main halo with a low figure rotation, and after its second pericentric passage becomes radially aligned at all subsequent times except at its third pericentric passage. The loss of alignment at pericentric passages is common in our sample (see Figure 3.12), and has been seen before by Kuhlen, Diemand & Madau (2007), Pereira, Bryan & Gill (2008), and Knebe et al. (2010), who all claim that the pericentric passage occurs so quickly that the subhalo does not have time to adjust its orientation to point toward the main halo.

It is interesting that it took two pericentric passages for this satellite to become aligned. Perhaps at P1 it did not come close enough to be affected tidally. Indeed, $V_{\rm max}$ did not decrease appreciably until just after P2 so the tidal effects at P1 may not have been strong enough to tidally torque (or stretch) the subhalo. Also note how the axis ratios b/a and c/a tend to increase after pericentric passages, confirming that tidal effects are indeed a likely cause of the circularisation of the internal structure of

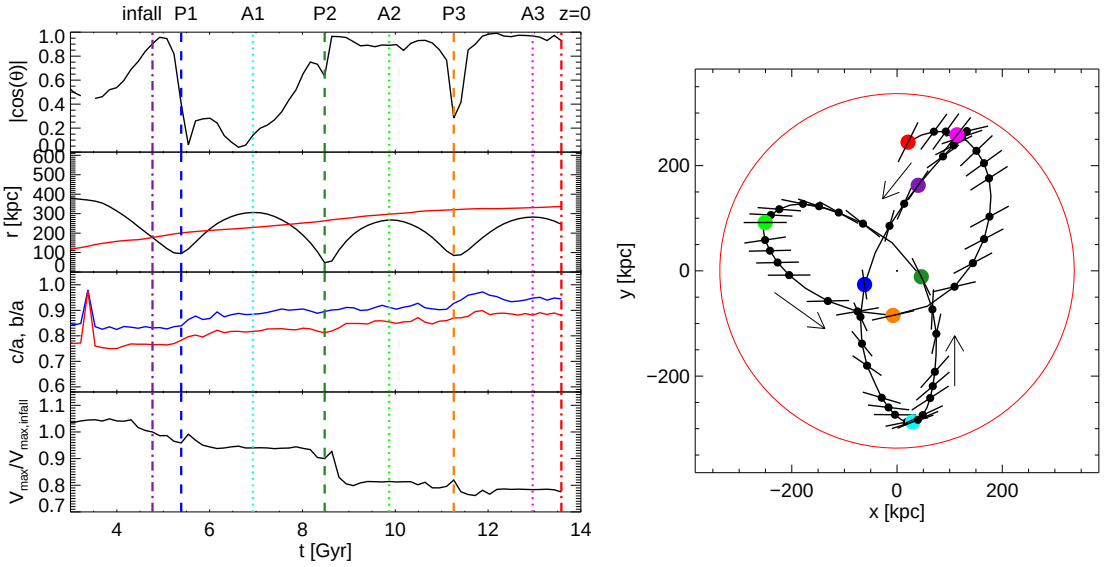

Figure 3.10: Example of a subhalo that becomes aligned with the main halo after infall. The left panels show alignment, orbital radius, axis ratios measured at 800 pc, and degree of stripping since infall as a function of time, from top to bottom respectively. Vertical lines indicate important points in the satellite's orbit; pericentres and apocentres are dashed and dotted, respectively. The right panel shows the orbit of this subhalo from 4 Gyr until $z = 0$, rotated to the orbital plane at $z = 0$. Black dots and lines indicate the direction of the subhalo's major axis projected onto the plane of the orbit. Each coloured dot corresponds to the time indicated by the vertical line of the same colour in the left panels. Arrows indicate the subhalo's velocity direction. The red circle indicates r_{200} of the main halo at $z = 0$.

these subhaloes.

Not all subhaloes experience alignment with the main halo, in spite of being tidally stripped. One such example is shown in Figure 3.11. After infall, this subhalo tumbles rapidly, possibly due to an interaction with another satellite, so quickly that it does not align despite a high degree of stripping and close pericentric passages. These results seem to corroborate the tidal torquing theory of Pereira, Bryan & Gill (2008): if a subhalo is initially tumbling very quickly, a much larger torque is required to slow it down enough to put in into a "tidally locked" orbit. This result is however in apparent contrast with Pereira & Bryan (2010) who find that satellites that are artificially given an initial figure rotation upon accretion are torqued into alignment within an orbital time. Because we have instead investigated this problem in a full cosmological simulation, we have revealed that many satellites have a high enough initial rotational speed that they are gyroscopically resistant to tidal torquing from

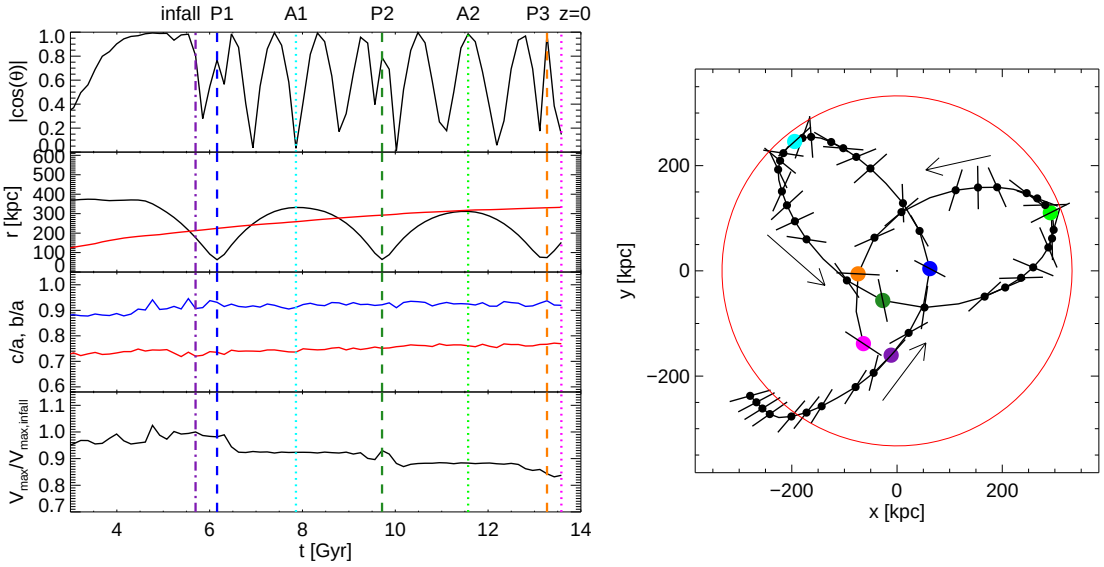

Figure 3.11: As in Figure 3.10 but now showing a subhalo that does not align due to a high initial figure rotation.

the main halo, and thus do not align even after several orbital times.

3.6.4 Alignment as a function of orbital phase

We find that many subhaloes tend to align after either their first or second pericentric passages. Therefore we now investigate the alignment as a function of orbital phase of all 43 satellites in our subsample. Histograms of the alignment at various orbital phases are shown in Figure 3.12. Note that the sample in each panel decreases with orbital time since some satellites have only recently been accreted and have not yet completed multiple orbits. At P1 and A1, most subhaloes have not yet aligned. However, after the 2nd pericentre, many subhaloes tend to align and remain aligned at subsequent apocentric passages. Alignment tends to be stronger at apocentre than pericentre, where alignment tend to be more randomized. Very few of these subhaloes have had more than 3 apocentric passages since infall, so we refrain from statistically investigating later orbital phases.

Note that this alignment almost always tends to follow extreme stripping events. In each panel of Figure 3.12 we show the mean degree of stripping since infall, defined as the ratio between $V_{\rm max}$ and that at infall, $V_{\rm max,infall}$. Most satellites experience their highest degree of stripping after the second pericentric passage, as the first is often not close enough to the centre of the main halo to experience significant mass loss,

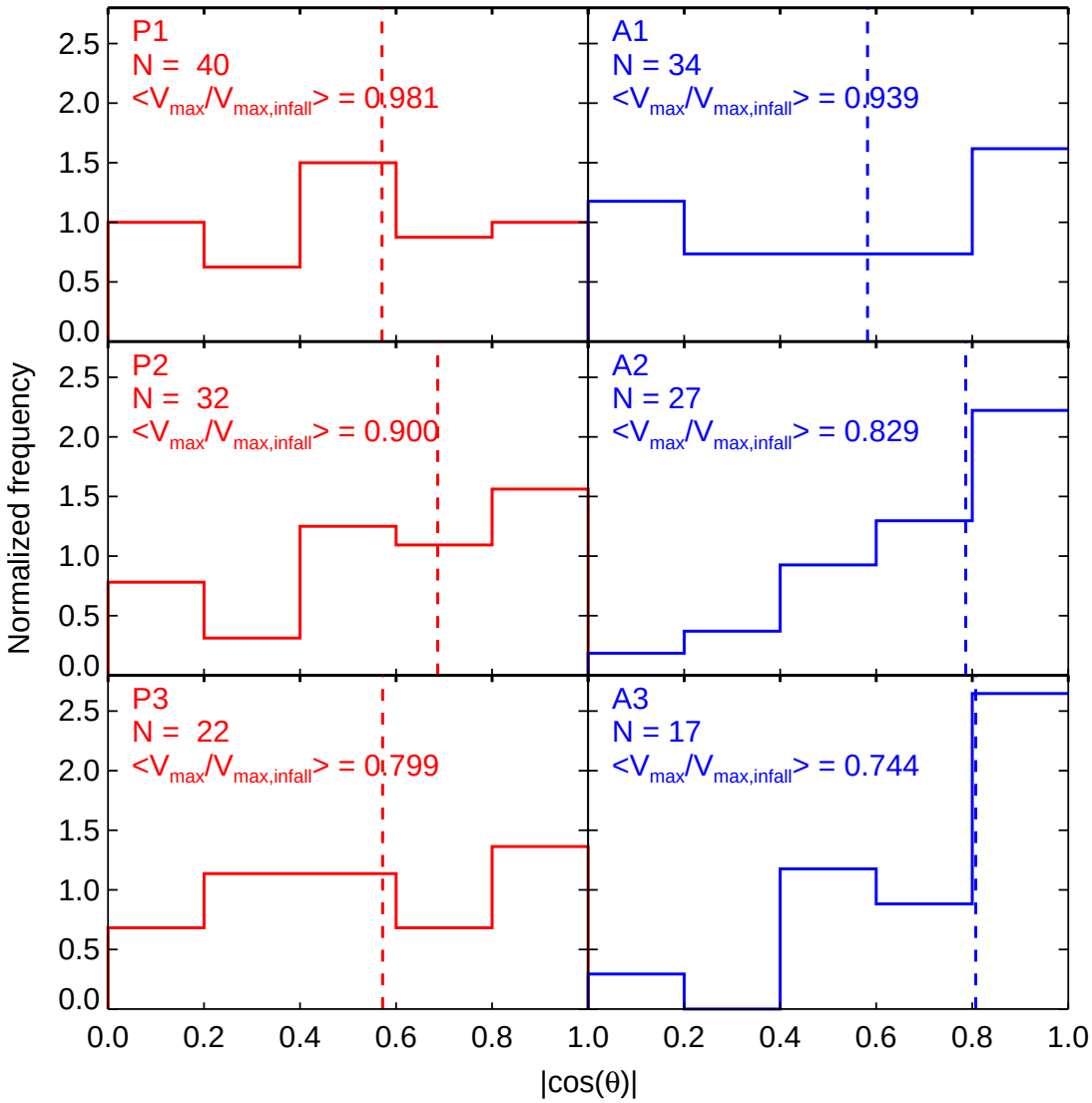

Figure 3.12: Alignment distributions of the major axis measured at 800 pc for those subhaloes shown in Figure 3.9, at various orbital phases. Medians are indicated by vertical dashed lines. Orbital phase is written in the top left portion of each panel as defined in Figure 3.10. The number of subhaloes and mean degree of stripping since infall are also indicated in the top left of each panel.

and the first passage tends to puff up the subhalo to make it easier to strip during the second pericentre passage (Nichols, Revaz & Jablonka, 2014). This correlation with stripping and radial alignment is very useful, since if one observes a satellite galaxy that is radially aligned with its host, there is a good chance that it has been around for at least two pericentric passages and has been tidally stripped by the main halo.

3.6.5 Alignment as a function of stripping

To investigate this correlation between radial alignment and stripping explicitly, in Figure 3.13 we show the alignment distribution of these 43 satellites in our subsample as a function of $V_{\rm max}/V_{\rm max,infall}$. For each panel we choose the same level of stripping as the mean ratio in the corresponding panel in Figure 3.12 to facilitate easier comparison between the two figures. At infall, before significant stripping can occur, the alignment distribution is already slightly skewed toward radial alignment. As subhaloes become stripped, their alignments become increasingly more randomized down to $V_{\rm max}/V_{\rm max,infall} = 0.9$. As stripping continues, the satellites begin to radially align strongly, especially below $V_{\rm max}/V_{\rm max,infall} = 0.83$.

Our finding that subhaloes are already aligned at infall has been seen in previous studies, and is thought to be caused by primordial alignment of haloes relative to the filaments in which they form due to torquing by the surrounding large-scale structure (Pereira, Bryan & Gill, 2008; Aragón-Calvo et al., 2007). As the subhaloes begin to be tidally stripped by the main halo, this primordial alignment is initially erased. However, over time the tidal field of the main halo causes the satellites to realign, and remain aligned throughout their orbits.

Even though we see a strong correlation between alignment and degree of stripping, it is likely that these highly stripped subhaloes have also been strongly torqued by the tidal field of the main halo. This degeneracy between stripping and tidal torquing makes it non-trivial to determine which process, if either, is the direct cause of this radial alignment. However, we find that subhaloes do not align until they have been significantly stripped ($V_{\rm max}/V_{\rm max,infall} < 0.83$); at this point they have lost over 70 per cent of their mass since infall. This, coupled with the fact that only slow rotators experience radial alignment despite significant stripping, leads us to believe that tidal torquing is the more likely direct cause of this alignment, while stripping is simply a side effect of the extreme tidal field required to torque the satellites.

Nevertheless, this correlation between alignment and stripping will be extremely useful for models of galaxy formation. For instance, if satellite galaxies of a given system are observationally found to be significantly aligned toward the centre of their host, it is likely that these satellite galaxies have undergone significant tidal stripping and thus must have formed within much larger haloes than the ones they currently occupy.

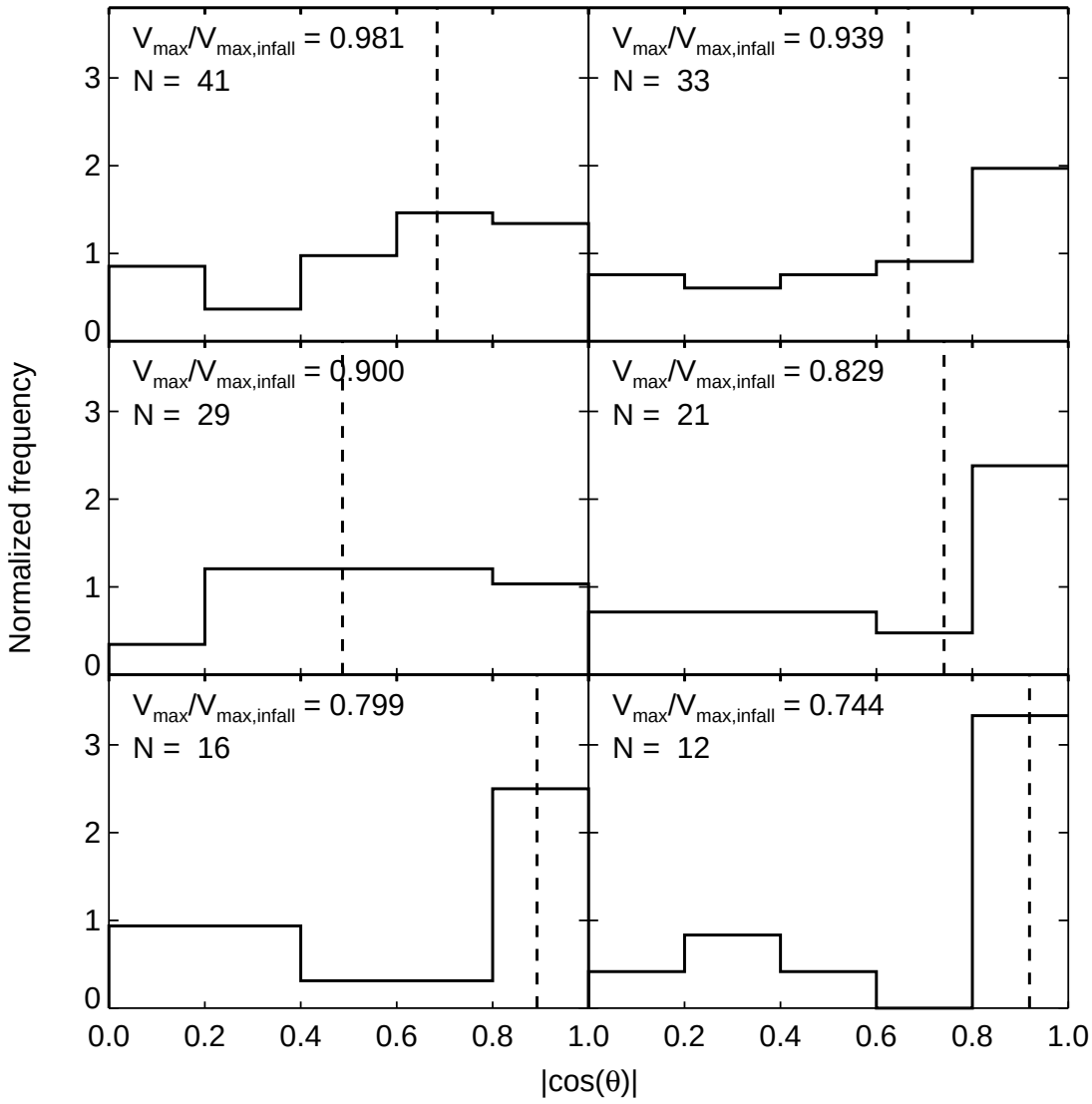

Figure 3.13: Alignment distributions of the major axis measured at 800 pc for those subhaloes shown in Figure 3.9, for various levels of stripping since infall as indicated in each panel. Medians are indicated by vertical dashed lines. The number of subhaloes is also indicated in the top left of each panel.

3.7 Discussion

We have shown that tidal effects cause satellite galaxies of MW-sized haloes to become more spherical and to radially align with the host over time.

This finding is quite interesting since most tidally stripped satellites of the MW have long, extended tails of stars extending across the sky. One famous example is

the Sagittarius stream that wraps around the MW several times. Therefore, naively, one would expect stripping to stretch and elongate subhaloes tangentially to our line of sight, rather than make them rounder and oriented radially. This apparent contradiction is explained by the fact that subhaloes are stripped from the outside in. These unbound streams of particles originate from the outskirts of the subhalo where the tidal forces are strongest, while the inner regions remain bound. Thus while the outer parts of a satellite become stripped and form long tidal tails along the progenitor's orbit, the surviving inner regions actually become more spherical and align radially with the host, until they too are stripped away.

With this information it should be possible to infer the dynamical history of a dSph galaxy orbiting a larger system by measuring its triaxiality and orientation relative to the host. If the kinematics of stars in a satellite are consistent with living in a triaxial dark matter halo, it is likely that the halo has not been significantly stripped.

Jeans modelling is often used to infer the underlying dark matter distribution based on the positions and line-of-sight velocities of stars in dSphs. However such models often make simplifying assumptions about the underlying system, such as the fact that the system is spherically symmetric. We find that the velocity dispersion along the major axes of our classical haloes with $c/a < 0.8$ is on average 10 per cent larger than along the minor axis. If dSphs tend to have their major axes oriented along the line of sight, as we have found here, spherically symmetric Jeans modeling may overestimate their masses. Indeed, through axisymmetric mass modelling, Hayashi & Chiba (2012) find the masses of some MW dSphs to be factors of a few smaller than when assuming spherical symmetry.

A major caveat is that, observationally, we do not have 3D spatial information of a galaxy. Everything is seen in projection onto the sky. Therefore it is quite difficult to make quantitative comparisons between our findings and observations. For instance, from our vantage point in the Galaxy it is nearly impossible to measure the Galactocentric radial extent of dSph satellites of the MW. Thus the radial alignment effect we measure here is difficult to confirm observationally in this regime. However this effect has been observed in the isophotal contours of satellites of galaxy clusters and groups on larger scales. Models of such systems must take into account a general radial alignment with the main halo. This could be especially important in weak-lensing surveys which rely on the assumption that satellites are oriented randomly with respect to their host (Smith et al., 2001; McKay et al., 2001). For example, Schneider

et al. (2013) estimate that intrinsic alignments between galaxy group members may contribute a systematic uncertainty of up to 20 per cent in the mean differential projected surface mass density of galaxy groups inferred from weak lensing observations. A thorough understanding of these radial alignments is thus crucial for the calibration of weak lensing measurements.

3.8 Conclusions

We have used the Aquarius simulation suite to investigate the shape and orientation of isopotential contours in dark matter haloes likely to contain classical ($M_V < -8$) dwarf spheroidal (dSph) galaxies similar to those found in the Local Group (referred to as "classical haloes"). Such contours are very well fit by triaxial ellipsoids. Convergence tests indicate that the axis ratios are accurate to better than 5% down to a convergence radius of $r_{\rm conv}(\kappa = 0.1) \approx 160$ pc at the level-2 resolution level of Aquarius. This excellent resolution allows us to probe the dark matter potential in these systems down to the typical half-light radii of dSph galaxies.

The shape of the potential is quite triaxial in the centre of classical haloes and becomes more spherical with radius. We find that classical subhaloes of the main MW-sized halo tend to be much more spherical than field haloes of comparable luminosity. This effect is seen at all radii, even at the typical half-light radii of MW dSph galaxies. Strong correlation is seen between sphericity and mass lost since infall, indicating that interactions with the tidal field of the host halo are the likely cause of the circularisation of the gravitational potential in subhaloes. This effect is measurable down to the half-light radii of typical MW dSph galaxies, and therefore should be observable in real systems. With the recently launched Gaia telescope, precise LOS motion and proper motions of stars in MW dSphs will allow better constraints on the shape of their gravitational potentials, thus allowing direct comparison with this work.

The orientation of classical satellites of MW-sized haloes was also measured. We find significant alignment between the major axes of the satellites and the direction to the host halo (median $|\cos(\theta)| = 0.75$), an effect that is independent of the radius at which the potential is measured. Subhaloes were tracked back in time to investigate the cause of such an alignment. Infalling subhaloes have a net preference for radial alignment possibly due to primordial torquing of the large scale structure. Interactions with the main halo erase this initial alignment, but subsequent close pericentric

passages strip and possibly torque subhaloes, realigning many of them toward the centre of the main halo. This alignment tends to occur after first or second pericentric passage and persists for the rest of the orbit, except at subsequent pericentric passages. These findings corroborate the tidal torquing theory of Pereira, Bryan & Gill (2008), where a satellite can be torqued into a locked orbit by the tidal field of the host. However, we find that only satellites with a low initial figure rotation can be efficiently torqued into permanent alignment.

Our vantage point in the Galaxy currently precludes the measurement of the Galactocentric radial extent of the MW dSphs, and thus a direct comparison of our orientation results to our own Galaxy is difficult. Studies like this will, however, be able to inform the calibration of weak lensing surveys that usually assume that satellite galaxies are oriented randomly relative to their host.

Chapter 4

Conclusions

We have studied dwarf satellite galaxies of Milky Way-sized dark matter haloes as predicted by the ΛCDM cosmological model coupled with a semi-analytic model of galaxy formation. We have studied two of their major properties:

1. The ellipticity of their orbits
2. The shape and orientation of the gravitational potential in the inner regions, where the luminous component of the galaxies is expected to exist

The major results can be summarized as follows:

- The orbital ellipticity distribution of luminous subhaloes exhibits little scatter between Aquarius main haloes, despite a large range in virial mass ($M_{200} = (0.8 - 1.8) \times 10^{12}\,\mathrm{M}_{\odot}$) and formation history. This finding makes the ellipticity distribution a robust prediction of the properties of satellite galaxies in ΛCDM.
- Luminous subhaloes are on much more elliptical orbits than their "dark" counterparts. This trend is primarily due to the fact that luminous subhaloes tend to be more massive than dark subhaloes, and thus experience different dynamical evolution after accretion onto the main halo. Specifically, this result is due to:

    1. Interactions between low and high mass subhaloes after accretion. The high mass subhaloes are affected very little by such interactions, while the low mass subhaloes either scatter to large radii (beyond the virial radius and are lost), or are scattered onto more circular orbits and remain within the virial radius.

2. An anticorrelation in orbital ellipticity at accretion with infall time, coupled with the fact that luminous satellites tend to accrete earlier than dark subhaloes on average.

- The computed orbital ellipticities of MW satellites are very sensitive to the assumed MW mass. The best match between the ellipticity distribution of the MW dSphs and Aquarius classical subhaloes is obtained for a MW mass of $1.1 \times 10^{12}\,\mathrm{M}_{\odot}$. Our results suggest, to 95% confidence, a MW mass between $0.6-3.1\times10^{12}\,\mathrm{M}_{\odot}$, in agreement with current estimates based on other methods (e.g. the timing argument and kinematics of blue horizontal branch stars in main halo).

- The excellent resolution of Level-2 Aquarius allows us, for the first time, to reliably measure the shape of the gravitational potential in luminous subhaloes down to $160h^{-1}$ pc, well within the typical half light radius of most MW dSph galaxies.

- The shape of the gravitational potential in field haloes tends to be triaxial in general, with maximal triaxiality in the innermost regions.

- Subhaloes of MW-sized haloes are more spherical than field haloes. This sphericalization is caused by tidal interactions with the main halo; sphericity increases with increased tidal mass loss.

- The major axes of luminous satellites are significantly aligned with the direction to the centre of the main halo. This bias is caused by interactions of the subhaloes with the host tidal field at close pericentric passages.

- Radial alignment will not occur if the infalling satellite is initially tumbling on a timescale much shorter than its typical orbital period. This new finding will help to better constrain tidal torquing theories of satellite galaxies.

These results were obtained through the analysis of the Aquarius Project, a cosmological Λ cold dark matter simulation suite of six Milky Way-sized haloes (Springel et al., 2008). By combining Aquarius with a semi-analytic model of galaxy formation and evolution (Starkenburg et al., 2013), we were able to identify the substructure of these MW-sized haloes likely to contain a stellar mass similar to the dwarf

spheroidal galaxies of the Local Group. The state-of-the-art time and spatial resolution of Aquarius allowed us to track these subhaloes through time, and to probe their internal structure down to very small radii, where the stellar content is expected to be found.

In this study, we have made robust predictions for the properties of dwarf spheroidal galaxies of the Milky Way. Through comparison with observations, one may thus place interesting constraints on the Local Group, such as the dynamical histories of the MW dSphs and the total mass of the MW itself. It is robust predictions like these that will help us test models of galaxy formation and cosmology on small scales in order to help finally put to rest some of the heated debates in this regime.

4.1 Outlook

The mass of the MW estimated in this thesis has a very large uncertainty. The error here is dominated by the fact that 1) we only have reliable proper motions for nine MW dSphs, and 2) the proper motions that we *do* have are quite uncertain. Fortunately, the recently launched ESA mission Gaia will measure proper motions of stars within many more dSphs and to much higher accuracy than is currently possible. Additionally, modern adaptive optics systems promise to provide ground-based telescopes with angular resolutions comparable to HST, with expected astrometric errors below the milliarcsecond level (Rigaut et al., 2012). With these improvements, this method of measuring the MW mass via a comparison between the ellipticity distributions of luminous satellites in simulations with that inferred for the MW dSphs will become much more precise, making this novel, independent approach of measuring the MW mass an excellent contender with other more established methods in the next few years.

One of the major caveats in this thesis is that the Aquarius haloes are isolated, with no other large objects within several Mpc. Indeed, the MW has a massive nearby companion: The Andromeda Galaxy (M31), roughly 785 kpc distant (McConnachie et al., 2005). Because some dSphs considered in this thesis range in distances from the MW of up to several hundred kpc (eg. Leo I is 258 kpc from the MW; McConnachie, 2012), it is possible that the total gravitational potential of the Local Group should be taken into account in our simulations in order to make accurate predictions of the MW dSphs. For example, it would be very interesting to see if the satellite ellipticity distribution is significantly different for a MW-sized halo in a Local Group

environment, rather than in isolation as was done here. We note that we do not expect this assumption to be a dominant source of error in our MW estimate, given the extremely large uncertainties in the dSph proper motions.

Bibliography

Abadi M. G., Navarro J. F., Fardal M., Babul A., Steinmetz M., 2010, MNRAS, 407, 435

Adami C., Gavazzi R., Cuillandre J. C., Durret F., Ilbert O., Mazure A., Pelló R., Ulmer M. P., 2009, A&A, 493, 399

Adén D. et al., 2009, A&A, 506, 1147

Agustsson I., Brainerd T. G., 2006, ApJ, 644, L25

Allgood B., Flores R. A., Primack J. R., Kravtsov A. V., Wechsler R. H., Faltenbacher A., Bullock J. S., 2006, MNRAS, 367, 1781

Angulo R. E., Springel V., White S. D. M., Jenkins A., Baugh C. M., Frenk C. S., 2012, MNRAS, 426, 2046

Aragón-Calvo M. A., van de Weygaert R., Jones B. J. T., van der Hulst J. M., 2007, ApJ, 655, L5

Balogh M. L., Navarro J. F., Morris S. L., 2000, ApJ, 540, 113

Barber C., Starkenburg E., Navarro J. F., McConnachie A. W., Fattahi A., 2014, MNRAS, 437, 959

Battaglia G., Helmi A., Breddels M., 2013, New A Rev., 57, 52

Battaglia G. et al., 2005, MNRAS, 364, 433

Battaglia G., Tolstoy E., Helmi A., Irwin M., Parisi P., Hill V., Jablonka P., 2011, MNRAS, 411, 1013

Baugh C. M., 2006, Reports on Progress in Physics, 69, 3101

Bellazzini M., Gennari N., Ferraro F. R., 2005, MNRAS, 360, 185

Bellazzini M., Gennari N., Ferraro F. R., Sollima A., 2004, MNRAS, 354, 708

Belokurov V. et al., 2007, ApJ, 654, 897

Benítez-Llambay A., Navarro J. F., Abadi M. G., Gottlöber S., Yepes G., Hoffman Y., Steinmetz M., 2013, ApJ, 763, L41

Benson A. J., 2010, Phys. Rep., 495, 33

Bernstein G. M., Norberg P., 2002, AJ, 124, 733

Blumenthal G. R., Faber S. M., Primack J. R., Rees M. J., 1984, Nature, 311, 517

Boylan-Kolchin M., Bullock J. S., Kaplinghat M., 2011, MNRAS, 415, L40

—, 2012a, MNRAS, 422, 1203

Boylan-Kolchin M., Bullock J. S., Sohn S. T., Besla G., van der Marel R. P., 2013, ApJ, 768, 140

Boylan-Kolchin M., Springel V., White S. D. M., Jenkins A., 2010, MNRAS, 406, 896

Breddels M. A., Helmi A., van den Bosch R. C. E., van de Ven G., Battaglia G., 2013, MNRAS, 433, 3173

Brown T. M. et al., 2012, ApJ, 753, L21

Burkert A., 1995, ApJ, 447, L25

Carrera R., Aparicio A., Martínez-Delgado D., Alonso-García J., 2002, AJ, 123, 3199

Clementini G., Gratton R., Bragaglia A., Carretta E., Di Fabrizio L., Maio M., 2003, AJ, 125, 1309

Colín P., Valenzuela O., Avila-Reese V., 2008, ApJ, 673, 203

Croton D. J. et al., 2006, MNRAS, 365, 11

Davis M., Efstathiou G., Frenk C. S., White S. D. M., 1985, ApJ, 292, 371

De Lucia G., Blaizot J., 2007, MNRAS, 375, 2

De Lucia G., Helmi A., 2008, MNRAS, 391, 14

De Lucia G., Kauffmann G., White S. D. M., 2004, MNRAS, 349, 1101

Deason A. J. et al., 2012, MNRAS, 425, 2840

Diemand J., Kuhlen M., Madau P., 2007, ApJ, 667, 859

Diemand J., Kuhlen M., Madau P., Zemp M., Moore B., Potter D., Stadel J., 2008, Nature, 454, 735

Djorgovski S., 1983, ApJ, 274, L7

D'Onghia E., Springel V., Hernquist L., Keres D., 2010, ApJ, 709, 1138

Eke V. R., Cole S., Frenk C. S., 1996, MNRAS, 282, 263

Faltenbacher A., Jing Y. P., Li C., Mao S., Mo H. J., Pasquali A., van den Bosch F. C., 2008, ApJ, 675, 146

Faltenbacher A., Li C., Mao S., van den Bosch F. C., Yang X., Jing Y. P., Pasquali A., Mo H. J., 2007, ApJ, 662, L71

Fukushige T., Makino J., 1997, ApJ, 477, L9

Gao L., De Lucia G., White S. D. M., Jenkins A., 2004, MNRAS, 352, L1

Garrison-Kimmel S., Rocha M., Boylan-Kolchin M., Bullock J. S., Lally J., 2013, MNRAS, 433, 3539

Ghigna S., Moore B., Governato F., Lake G., Quinn T., Stadel J., 1998, MNRAS, 300, 146

Gill S. P. D., Knebe A., Gibson B. K., 2005, MNRAS, 356, 1327

Gill S. P. D., Knebe A., Gibson B. K., Dopita M. A., 2004, MNRAS, 351, 410

Gilmore G., Wilkinson M., Kleyna J., Koch A., Evans W., Wyse R. F. G., Grebel E. K., 2007, Nuclear Physics B Proceedings Supplements, 173, 15

Gott, III J. R., Rees M. J., 1975, A&A, 45, 365

Governato F. et al., 2010, Nature, 463, 203

Guo Q., White S., Angulo R. E., Henriques B., Lemson G., Boylan-Kolchin M., Thomas P., Short C., 2013, MNRAS, 428, 1351

Harris J., Zaritsky D., 2006, AJ, 131, 2514

Hartwick F. D. A., Sargent W. L. W., 1978, ApJ, 221, 512

Hawley D. L., Peebles P. J. E., 1975, AJ, 80, 477

Hayashi E., Navarro J. F., Springel V., 2007, MNRAS, 377, 50

Hayashi K., Chiba M., 2012, ApJ, 755, 145

Hung C.-L., Ebeling H., 2012, MNRAS, 421, 3229

Ibata R. A., Gilmore G., Irwin M. J., 1994, Nature, 370, 194

Irwin M., Hatzidimitriou D., 1995, MNRAS, 277, 1354

Irwin M. J. et al., 2007, ApJ, 656, L13

Jing Y. P., Suto Y., 2002, ApJ, 574, 538

Kauffmann G., Colberg J. M., Diaferio A., White S. D. M., 1999, MNRAS, 303, 188

Kazantzidis S., Abadi M. G., Navarro J. F., 2010, ApJ, 720, L62

Kirby E. N., Simon J. D., Geha M., Guhathakurta P., Frebel A., 2008, ApJ, 685, L43

Kleyna J., Wilkinson M. I., Evans N. W., Gilmore G., Frayn C., 2002, MNRAS, 330, 792

Klypin A., Gottlöber S., Kravtsov A. V., Khokhlov A. M., 1999a, ApJ, 516, 530

Klypin A., Kravtsov A. V., Valenzuela O., Prada F., 1999b, ApJ, 522, 82

Knebe A., Draganova N., Power C., Yepes G., Hoffman Y., Gottlöber S., Gibson B. K., 2008, MNRAS, 386, L52

Knebe A., Libeskind N. I., Knollmann S. R., Yepes G., Gottlöber S., Hoffman Y., 2010, MNRAS, 405, 1119

Kochanek C. S., 1996, ApJ, 457, 228

Koposov S. et al., 2008, ApJ, 686, 279

Kravtsov A. V., Gnedin O. Y., Klypin A. A., 2004, ApJ, 609, 482

Kuhlen M., Diemand J., Madau P., 2007, ApJ, 671, 1135

Kulessa A. S., Lynden-Bell D., 1992, MNRAS, 255, 105

Kuzio de Naray R., McGaugh S. S., 2014, ArXiv e-prints

Lépine S., Koch A., Rich R. M., Kuijken K., 2011, ApJ, 741, 100

Li Y., De Lucia G., Helmi A., 2010, MNRAS, 401, 2036

Li Y.-S., Helmi A., De Lucia G., Stoehr F., 2009, MNRAS, 397, L87

Li Y.-S., White S. D. M., 2008, MNRAS, 384, 1459

Lindegren L., Perryman M. A. C., 1996, A&AS, 116, 579

Lovell M. R. et al., 2012, MNRAS, 420, 2318

Ludlow A. D., Navarro J. F., Springel V., Jenkins A., Frenk C. S., Helmi A., 2009, ApJ, 692, 931

Lux H., Read J. I., Lake G., 2010, MNRAS, 406, 2312

Lynden-Bell D., Cannon R. D., Godwin P. J., 1983, MNRAS, 204, 87P

Macciò A. V., Ruchayskiy O., Boyarsky A., Muñoz-Cuartas J. C., 2013, MNRAS, 428, 882

Mamon G. A., Sanchis T., Salvador-Solé E., Solanes J. M., 2004, A&A, 414, 445

Martin N. F., de Jong J. T. A., Rix H.-W., 2008, ApJ, 684, 1075

Mateo M., Olszewski E. W., Walker M. G., 2008, ApJ, 675, 201

Mateo M. L., 1998, ARA&A, 36, 435

Mayer L., Kazantzidis S., Mastropietro C., Wadsley J., 2007, Nature, 445, 738

McConnachie A. W., 2012, AJ, 144, 4

McConnachie A. W., Irwin M. J., Ferguson A. M. N., Ibata R. A., Lewis G. F., Tanvir N., 2005, MNRAS, 356, 979

McConnachie A. W. et al., 2009, Nature, 461, 66

McKay T. A. et al., 2001, ArXiv Astrophysics e-prints

McMillan P. J., 2011, MNRAS, 418, 1565

Monaco L., Bellazzini M., Ferraro F. R., Pancino E., 2004, MNRAS, 353, 874

Moore B., 1994, Nature, 370, 629

Moore B., Ghigna S., Governato F., Lake G., Quinn T., Stadel J., Tozzi P., 1999, ApJ, 524, L19

Navarro J. F., Eke V. R., Frenk C. S., 1996, MNRAS, 283, L72

Navarro J. F., Frenk C. S., White S. D. M., 1996, ApJ, 462, 563

—, 1997, ApJ, 490, 493

Navarro J. F. et al., 2010, MNRAS, 402, 21

Neto A. F. et al., 2007, MNRAS, 381, 1450

Nichols M., Lin D., Bland-Hawthorn J., 2012, ApJ, 748, 149

Nichols M., Revaz Y., Jablonka P., 2014, ArXiv e-prints

Norris J. E., Wyse R. F. G., Gilmore G., Yong D., Frebel A., Wilkinson M. I., Belokurov V., Zucker D. B., 2010, ApJ, 723, 1632

Pasetto S., Grebel E. K., Berczik P., Chiosi C., Spurzem R., 2011, A&A, 525, A99

Peñarrubia J., Pontzen A., Walker M. G., Koposov S. E., 2012, ApJ, 759, L42

Peebles P. J. E., 1969, ApJ, 155, 393

Pereira M. J., Bryan G. L., 2010, ApJ, 721, 939

Pereira M. J., Bryan G. L., Gill S. P. D., 2008, ApJ, 672, 825

Pereira M. J., Kuhn J. R., 2005, ApJ, 627, L21

Perlmutter S. et al., 1999, ApJ, 517, 565

Piatek S., Pryor C., Bristow P., Olszewski E. W., Harris H. C., Mateo M., Minniti D., Tinney C. G., 2005, AJ, 130, 95

—, 2006, AJ, 131, 1445

—, 2007, AJ, 133, 818

Piatek S., Pryor C., Olszewski E. W., 2008, AJ, 135, 1024

Piatek S. et al., 2002, AJ, 124, 3198

Piatek S., Pryor C., Olszewski E. W., Harris H. C., Mateo M., Minniti D., Tinney C. G., 2003, AJ, 126, 2346

Pietrzyński G. et al., 2008, AJ, 135, 1993

Pietrzyński G., Górski M., Gieren W., Ivanov V. D., Bresolin F., Kudritzki R.-P., 2009, AJ, 138, 459

Planck Collaboration et al., 2013, ArXiv e-prints

Power C., Navarro J. F., Jenkins A., Frenk C. S., White S. D. M., Springel V., Stadel J., Quinn T., 2003, MNRAS, 338, 14

Press W. H., Schechter P., 1974, ApJ, 187, 425

Pryor C., Piatek S., Olszewski E. W., 2010, AJ, 139, 839

Read J. I., Gilmore G., 2005, MNRAS, 356, 107

Rigaut F. et al., 2012, in Society of Photo-Optical Instrumentation Engineers (SPIE) Conference Series, Vol. 8447, Society of Photo-Optical Instrumentation Engineers (SPIE) Conference Series

Sales L. V., Navarro J. F., Abadi M. G., Steinmetz M., 2007a, MNRAS, 379, 1464

Schneider M. D. et al., 2013, MNRAS, 433, 2727

Schneider M. D., Frenk C. S., Cole S., 2012, J. Cosmology Astropart. Phys., 5, 30

Schönrich R., Binney J., Dehnen W., 2010, MNRAS, 403, 1829

Simon J. D. et al., 2011, ApJ, 733, 46

Smith D. R., Bernstein G. M., Fischer P., Jarvis M., 2001, ApJ, 551, 643

Smith M. C. et al., 2007, MNRAS, 379, 755

Sohn S. T., Besla G., van der Marel R. P., Boylan-Kolchin M., Majewski S. R., Bullock J. S., 2013, ApJ, 768, 139

Springel V. et al., 2008, MNRAS, 391, 1685

Springel V., White S. D. M., Hernquist L., 2004, in IAU Symposium, Vol. 220, Dark Matter in Galaxies, Ryder S., Pisano D., Walker M., Freeman K., eds., p. 421

Springel V. et al., 2005, Nature, 435, 629

Springel V., White S. D. M., Tormen G., Kauffmann G., 2001, MNRAS, 328, 726

Stadel J., Potter D., Moore B., Diemand J., Madau P., Zemp M., Kuhlen M., Quilis V., 2009, MNRAS, 398, L21

Starkenburg E. et al., 2013, MNRAS, 429, 725

Steigman G., 2007, Annual Review of Nuclear and Particle Science, 57, 463

Stoehr F., White S. D. M., Tormen G., Springel V., 2002, MNRAS, 335, L84

Strigari L. E., Bullock J. S., Kaplinghat M., Diemand J., Kuhlen M., Madau P., 2007, ApJ, 669, 676

Strigari L. E., Bullock J. S., Kaplinghat M., Simon J. D., Geha M., Willman B., Walker M. G., 2008, Nature, 454, 1096

Strigari L. E., Frenk C. S., White S. D. M., 2010, MNRAS, 408, 2364

Taffoni G., Mayer L., Colpi M., Governato F., 2003, MNRAS, 341, 434

Teyssier M., Johnston K. V., Kuhlen M., 2012, MNRAS, 426, 1808

Teyssier R., Pontzen A., Dubois Y., Read J. I., 2013, MNRAS, 429, 3068

Tolstoy E., Hill V., Tosi M., 2009, ARA&A, 47, 371

Tormen G., 1997, MNRAS, 290, 411

Tormen G., Diaferio A., Syer D., 1998, MNRAS, 299, 728

Udalski A., Szymanski M., Kubiak M., Pietrzynski G., Soszynski I., Wozniak P., Zebrun K., 1999, Acta Astron., 49, 201

van den Bosch F. C., Lewis G. F., Lake G., Stadel J., 1999, ApJ, 515, 50

van der Marel R. P., Alves D. R., Hardy E., Suntzeff N. B., 2002, AJ, 124, 2639

Vera-Ciro C. A., 2013, PhD thesis, University of Groningen

Vera-Ciro C. A., Helmi A., Starkenburg E., Breddels M. A., 2013, MNRAS, 428, 1696

Vera-Ciro C. A., Sales L. V., Helmi A., Frenk C. S., Navarro J. F., Springel V., Vogelsberger M., White S. D. M., 2011, MNRAS, 416, 1377

Viel M., Lesgourgues J., Haehnelt M. G., Matarrese S., Riotto A., 2005, Phys. Rev. D, 71, 063534

Walker M., 2013, Dark Matter in the Galactic Dwarf Spheroidal Satellites, Oswalt T. D., Gilmore G., eds., Springer Science+Business Media Dordrecht, p. 1039

Walker M. G., Mateo M., Olszewski E. W., 2009a, AJ, 137, 3100

Walker M. G., Mateo M., Olszewski E. W., Gnedin O. Y., Wang X., Sen B., Woodroofe M., 2007, ApJ, 667, L53

Walker M. G., Mateo M., Olszewski E. W., Peñarrubia J., Wyn Evans N., Gilmore G., 2009, ApJ, 704, 1274

—, 2009b, ApJ, 704, 1274

Walker M. G., Peñarrubia J., 2011, ApJ, 742, 20

Walsh S. M., Jerjen H., Willman B., 2007, ApJ, 662, L83

Wang H., Mo H. J., Jing Y. P., 2009, MNRAS, 396, 2249

Wang J., De Lucia G., Kitzbichler M. G., White S. D. M., 2008, MNRAS, 384, 1301

Wang J., Frenk C. S., Navarro J. F., Gao L., Sawala T., 2012, MNRAS, 424, 2715

Wang J., White S. D. M., 2009, MNRAS, 396, 709

Watkins L. L., Evans N. W., An J. H., 2010, MNRAS, 406, 264

Wetzel A. R., 2011, MNRAS, 412, 49

White S. D. M., Rees M. J., 1978, MNRAS, 183, 341

Wilkinson M. I., Evans N. W., 1999, MNRAS, 310, 645

Willman B. et al., 2005, AJ, 129, 2692

Wolf J., Martinez G. D., Bullock J. S., Kaplinghat M., Geha M., Muñoz R. R., Simon J. D., Avedo F. F., 2010, MNRAS, 406, 1220

Xue X. X. et al., 2008, ApJ, 684, 1143

York D. G. et al., 2000, AJ, 120, 1579

Zaritsky D., Olszewski E. W., Schommer R. A., Peterson R. C., Aaronson M., 1989, ApJ, 345, 759

Zucker D. B. et al., 2006b, ApJ, 650, L41

—, 2006a, ApJ, 643, L103